

Multi-scale analysis of magnetic fields in filamentary molecular clouds in Orion A

Frédéric POIDEVIN

*Universidade de São Paulo, Instituto de Astronomia, Geofísica e Ciências Atmosféricas,
Rua do Matão 1226, Butantã, São Paulo, SP 05508-900, Brazil*

Poidevin@astro.iag.usp.br

P. Bastien

*Département de Physique and Observatoire du Mont-Mégantic, Université de Montréal,
C.P. 6128, Succ. Centre-ville, Montréal, Québec H3C 3J7, Canada.*

Bastien@astro.umontreal.ca

T. J. Jones ¹

*University of Minnesota, Department of Astronomy, 116 Church St. S.E., Minneapolis,
MN 55455*

tjj@astro.umn.edu

ABSTRACT

New visible and K -band polarization measurements on stars surrounding molecular clouds in Orion A and stars in the BN vicinity are presented. Our results confirm that magnetic fields located inside the Orion A molecular clouds and in their close neighborhood are spatially connected. On and around the BN object, we measured the angular offsets between the K -band polarization data and available submm data. We find high values of the polarization degree, P_K , and of the optical depth, τ_K , close to an angular offset position of 90° whereas lower values of P_K and τ_K are observed for smaller angular offsets. We interpret these results as evidence for the presence of various magnetic field components toward lines of sight in the vicinity of BN. On a larger scale, we measured the distribution of angular offsets between available H -band polarization data and

¹Visiting Astronomer at the Infrared Telescope Facility which is operated by the University of Hawaii under contract from the National Aeronautics and Space Administration.

the same submm data set. Here we find an increase of $\langle P_H \rangle$ with angular offset which we interpret as a rotation of the magnetic field by $\lesssim 60^\circ$. This trend generalizes previous results on small scale toward and around lines of sight to BN and is consistent with a twist of the magnetic field on a larger scale towards OMC-1. A comparison of our results with several other studies suggests that a two-component magnetic field, maybe helical, could be wrapping the OMC-1 filament.

Subject headings: ISM: individual objects (Orion A, OMC-1, OMC-2, OMC-3, OMC-4) — ISM: magnetic fields — polarization

1. INTRODUCTION

In order to better understand the nature of magnetic fields observed in the diffuse interstellar medium (ISM) and in higher density regions of the ISM, we compare results from two observational techniques, visible and near-infrared (NIR) polarimetry of background stars and submillimeter (submm) polarimetry in dark clouds. Such a comparison between two different wavelength regimes was applied in a previous paper by Poidevin & Bastien (2006) to the GF 9 region. Here it is applied to the filamentary star-forming molecular clouds in the Orion A region.

Visible polarimetry by pioneers such as Hiltner (1949) and Hall & Mikesell (1949), followed by others such as Mathewson & Ford (1970), led to a first picture of the Galactic magnetic field assuming that dust grains pervading the diffuse ISM are magnetically aligned with their long axis preferentially perpendicular to the local magnetic field. In this context, polarization is produced by dichroic extinction. The second technique, polarimetry at longer wavelengths, successfully investigated in the far-infrared (FIR) by Cudlip et al. (1982), and in the submm by Hildebrand et al. (1984), allowed the first detections of the polarized radiation emitted by aligned dust grains in several cold dense regions in the ISM including OMC-1, thus probing magnetic fields in these environments. In parallel to improvements in both techniques, a general dust grain alignment theory was developed and is now arriving to maturity as reviewed by Lazarian (2003) and Lazarian (2007).

Since the advent of both techniques, several observations focused on the Orion region. The “Integral Shaped Filament” (ISF) observed at submm wavelengths by Johnstone & Bally (1999) is part of the molecular clouds located in the Barnard’s/Eridanus loop, a diffuse and expanding shell of enhanced optical emission covering an area of $\approx 15^\circ \times 8^\circ$. Located to the south of Orion B and to the north of the L1641 dark nebulae, the ISF lies in the northern

portion of Orion A which is one of the most active sites of star formation in the solar vicinity. It is associated with the well-known Orion nebula and the bright Trapezium stars. It also contains the OMC-1 cloud core located behind the nebula, the two extensively studied star-forming filaments, OMC-2 and OMC-3, located $\approx 15'$ and $25'$ to the north (see Castets & Langer 1995), IRAS 05327-0457 located $\approx 30'$ to the north and OMC-4 located $\approx 8'$ to the south (see Houde et al. 2004) of OMC-1.

A combination of 21 cm emission-line Zeeman splitting observations with a compilation of visible polarimetry by Heiles (1997) gives a relatively complex picture of the magnetic field on large spatial scales in the Eridanus/Orion region. On smaller spatial scales, visible polarimetry observations were carried out by Breger (1976) and Breger (1977) in the vicinity of Orion A. Based on these data the mean magnetic field projected on the plane-of-the-sky (POS) appears to be consistent with the picture of the magnetic field depicted within the clouds by Schleuning (1998) from $100\ \mu\text{m}$ and $350\ \mu\text{m}$ polarimetry in OMC-1. Polarimetry at $\lambda = 850\ \mu\text{m}$ by Matthews & Wilson (2000) and Matthews et al. (2001) shows that a helical magnetic field could thread the northern region of the OMC-3 dust filament. Additional polarimetry was obtained by Houde et al. (2004) at $\lambda = 350\ \mu\text{m}$ in OMC-2 and OMC-3 and by Poidevin et al. (2010) at $850\ \mu\text{m}$ in OMC-2. Comparison of these data revealed that the polarization patterns are fairly similar at both wavelengths. Poidevin et al. (2010) found that uniform magnetic field components are dominant compared to turbulent ones in OMC-3, but uniform and turbulent components are comparable in OMC-2.

The work proposed in the following is partially complementary to the one recently presented by Li et al. (2009) where a comparison of the magnetic fields probed at scales between the accumulation length and the size of cloud cores is discussed. Li et al. (2009) show that for field directions detected at the two extremes, a significant correlation is found. On the contrary Poidevin & Bastien (2006) find that the large scale uniform magnetic field observed in the vicinity of the GF-9 filaments could be dragged on smaller scale in one of the rotating cores. In order to improve our knowledge of the morphology of the magnetic fields on intermediate scales and its interpretation, new visible and NIR polarization observations are presented. These observations cover the Orion A region and its vicinity and compensate for the previous under-sampling of the magnetic field on scales of a few times the width of the ISF seen on submm emission maps (Johnstone & Bally 1999). This corresponds to a scale of $\approx 2.5\ \text{pc}$ on the POS for a distance to the Nebula of about $414\ \text{pc}$ (see Menten et al. 2007).

The new data with a compilation of published visible polarization data are presented in section 2. Submm, visible and NIR data are used in section 3 to compare the direction of magnetic fields projected on the POS as probed with the two techniques on spatial scales

ranging from $\approx 2^\circ$ to $\approx 1'$. This section is structured as follows: first a comparison of results on large spatial scales ($\approx 1^\circ \times 4^\circ$) is presented. Then regions OMC-1, OMC-2/3 and OMC-4 are discussed and compared to fields from large to small spatial scales when appropriate. NIR data in the Becklin-Neugebauer (BN) region are extensively analyzed and compared with submm polarimetry data. A discussion of the results follows in section 4 and a summary in section 5.

2. OBSERVATIONAL RESULTS

2.1. Visible Polarization Data in and around Orion A

2.1.1. Observations

Observations were carried out on the 1.6 m Ritchey-Chrétien telescope of the Observatoire du Mont-Mégantic (OMM), Québec, Canada, between 2003 January and 2004 November with Beauty and the Beast, a two-channel photoelectric polarimeter, which uses a Wollaston prism, a Pockels cell, and a quarter wave plate with a $8''.2$ aperture hole and a broad red filter (RG645: 7660 Å central wavelength, 2410 Å FWHM). The data were calibrated for instrumental efficiency, instrumental polarization (due to the telescope mirrors) and zero point of the position angles using a calibration prism, non polarized standard stars, and polarized standard stars, respectively. The instrumental polarization was measured to be $0.054 \pm 0.068\%$ and was subtracted from the observed polarization values. The observational errors were calculated from photon statistics and also include uncertainties introduced by the previously mentioned calibrations. The final uncertainty on individual measurements of the polarization P is usually around 0.1%. The data were de-biased in the standard way (e.g. Wardle & Kronberg 1974). More details about the instrument and the observational method can be found in Manset & Bastien (1995).

Additional polarimetry was obtained on 14 sources in OMC-2 during 1992 October at the Mount Lemmon Observing Facility (MLOF) $60''$ using the Two-Holer Photopolarimeter with Cousins-Kron V , R and I filters. A description of this instrument can be found in Sitko et al. (1985).

IR polarimetry on stars in OMC-1 near the BN object is described below in section 2.2.

2.1.2. *Compilation of the Data*

A set of 69 stars located throughout the whole Orion A region was observed at OMM. Among this set, 41 objects had never been observed before in polarimetry; these new data are presented in Table 1. Table 2 presents data on stars observed more than once, at OMM and published by Breger (1976) or found in the Heiles (2000) catalog. Table 3 presents data on other stars published by Breger (1976) or in the Heiles (2000) catalog. Following Breger (1976) the polarization mainly produced either by ISM dust or by Intracluster Dust (ICD) is indicated in the Tables. The effective wavelength of the stars observed by Breger (1976) lies between that of the B and V filters. On the other hand, wavelengths at which stars were observed are not specified in the Heiles (2000) catalog but in many cases the V filter was used. In each Table, Parenago and when available HD numbers for each star are shown in columns 1 and 2, respectively. Equatorial coordinates at epoch J2000.0 are given in columns 3 and 4. Measured polarization values with uncertainties, and position angles with their uncertainties are given in columns 5 to 8, respectively. Then ‘1’ is tabulated in column 9 if the signal to noise ratio $P/\sigma_P > 3$ (meaning $\sigma_\theta < 9.5^\circ$) otherwise ‘0’ is tabulated. Column 10 gives an approximate value of the visible absorption coefficient A_V from the Dobashi et al. (2005) catalog. This catalog is the first version of the atlas and catalog of dark clouds derived by using an optical star-count technique on the 1043 plates in the DSS. Distance estimates retrieved from the Heiles (2000) catalog are shown in column 11.

Polarization data for the stars observed from Mount Lemmon are compiled in Table 4. The identification number appearing in the first column is from Jones et al. (1994) where JHK photometry data are compiled in their Table 1. J2000.0 coordinates are given in columns 2 and 3. Results of the polarimetry in the three bands are given in columns 4 to 15. The extinction coefficient appearing in column 16 is from the Dobashi et al. (2005) catalog.

2.1.3. *Classification of the Data*

A quality code (SC) is shown in the last column of Tables 1, 2 and 3. The selection criteria used to classify the data, and to distinguish polarization produced by scattering on dust grains from polarization produced by dichroic extinction, are: ‘1’ is tabulated for data for which the polarization is produced by dichroic extinction with great reliability, meaning that (1) the position angles do not rotate more than 20° when observations are available at several wavelengths, or that (2) no variability of the degree of polarization and of the position angle can be found with time at a given wavelength. Some of the stars listed in Tables 2 or 3 are marked with ‘1’ following results from Breger (1976) and Breger (1977). The value ‘2’ is tabulated for (3) data with a position angle approximately the same as those

of reliable data in their vicinity. ‘?’ is tabulated for data for which we do not have enough information in light of the three conditions mentioned above, and ‘0’ is tabulated for data in contradiction with conditions (1) and (2). Finally, ‘0’ is systematically tabulated when the signal to noise ratio $P/\sigma_P < 3$. Following the analysis discussed in the next section (2.1.4), a few other stars also have their quality code forced to $SC = 0$.

The selection code shown in the last column of Table 4 follows the same conventions except that data with $P/\sigma_P < 3$ (meaning $\sigma_\theta > 9.5^\circ$) are also positively considered here since their signal-to-noise ratio is never far from the ratio $P/\sigma_P = 3$.

2.1.4. *Distribution of Visible Polarization with Visual Extinction*

The distribution of polarization, P , with visual extinction, A_V , is shown in Figure 1. The upper axis shows $E_{B-V} = A_V/R_V (= 3.1)$. The dashed line shows the limit (Serkowski et al. 1975) $P = 9E_{B-V} = 2.9A_V$ with the usual parameter $R = 3.1$. However, the mean of selective to total extinction ratios has been determined in Orion A by Ducati et al. (2003) to be $\bar{R} = 4.93 \pm 0.51$. The full line shows the limit $P = 9E_{B-V}$ when $\bar{R} = 4.93$ is used instead of the normal interstellar value. Dotted lines show the corresponding limits when uncertainties on \bar{R} are included. Crosses show reliable and less reliable data from Tables 1, 2 and 3 and diamonds show reliable and less reliable data from Table 4 where the R -filter data is used. We recall the A_V values come from Dobashi et al. (2005), are based on an optical star-count technique and therefore could be good estimators of the visible absorption along the LOSs to the observed stars or upper limits on the visible absorption along the LOSs to stars foreground to or poorly embedded into the cloud.

For this reason they do not depend on the value of R_V one may adopt. On the other hand, the value of R_V one may use gives upper limits on E_{B-V} . In the following we adopt the usual value of $R_V = 3.1$. We define $E_{B-V, \text{lim}} = A_V/3.1$ and reject data with $P_V > 9E_{B-V, \text{lim}} (= 2.9A_V)$.

Many points can be seen in Figure 1 above the upper limit $P = 2.9A_V$. Some of these objects are stars observed by Breger (1976) and references therein; their well characterized polarization measured at several epochs in several bands is produced by dichroic extinction by intra cluster dust (ICD) or by the foreground ISM according to his analysis. Therefore we chose to include it in our analysis. Objects not discussed by Breger (1976) are star P2244 and IR sources 175, 207 and 217 (see Table 4 and Jones et al. 1994). Multiwavelength observations shown in Table 4 suggest that polarization of objects 175 and 207 could be produced by dichroic absorption mechanisms; this would need to be confirmed by further

observations and we chose to exclude these objects from our analysis. Stars P2244 and IR source 217 were also removed from the sample.

In conclusion, all visible data displayed in Tables 1, 2, 3 and 4 are classified as follows: data defined as reliable to probe magnetic fields are data for which the selection code ‘1’ or ‘2’ is tabulated. Data considered as less reliable are marked with ‘?’. Data considered as unreliable are marked with ‘0’. In our analysis only reliable and less reliable data for probing magnetic fields are considered. In the rest of the paper, unless stated otherwise, the term reliable will be used to refer to the reliability with regards to probing magnetic fields as gauged by the selection code.

2.1.5. Visible Polarization Map and Histograms of Polarization Data

A polarization map of reliable and less reliable data from Tables 1, 2 or 3 is shown in Figure 2. When several measurements are available (see Tables 2 and 3), data with the best signal-to-noise ratio are shown in the Figure. The data cover an area of $\approx 1.5 \times 2.1$ centered on the region OMC-2, meaning an area of about $15 \text{ pc} \times 21 \text{ pc}$ for a distance to the Nebula of about 414 pc (see Menten et al. 2007). Histograms of polarization percentages and position angles of the data shown in Figure 2 are presented in Figures 3 and 4, respectively. In Figure 3, the mean and the dispersion of the whole data set ($N=94$) are $\bar{P} = 1.70\%$ and $S_P = 1.81\%$, respectively. Reliable data ($N=55$) are shown with full lines and the mean and the dispersion of this data set are $\bar{P} = 1.92\%$ and $S_P = 2.12\%$, respectively. The polarization position angle is a variable that wraps on over itself therefore the means retained in our analysis correspond to the means obtained where the dispersions of the distributions are found to be the smallest. In Figure 4, the mean and the dispersion of the whole data set are $\bar{\theta} = 75.0$ and $S_\theta = 36.5$, respectively. Reliable data are shown with full lines and the mean and the dispersion of this data set are $\bar{\theta} = 78.5$ and $S_\theta = 29.8$, respectively.

Reliable and less reliable data from Table 4 are shown in Figure 5. Also shown in the map are the data selected from Tables 1, 2 and 3 located in the region. Data from Table 4 cover an area of $\approx 0.2 \times 0.1$ (or about $2 \text{ pc} \times 1 \text{ pc}$ for a distance of about 414 pc to the Nebula (see Menten et al. 2007)) with six stars located in the LOSs to regions FIR3 to FIR6 (see Chini et al. 1997). Stars P2007 and P2029 from Table 1 are also located in similar LOSs. Following Jones et al. (1994), all the stars from Table 4 are brighter than $K = +13$ and are not field stars. They must be members of a young association or associations within the observed region. Histograms of polarization percentages and position angles of reliable and less reliable data from Table 4 are shown in Figures 6 and 7, respectively. In Figure 6, the mean and the dispersion of the whole data set ($N=11$) are $\bar{P} = 0.82\%$ and

$S_P = 0.97\%$, respectively. Reliable data only ($N=6$) are shown with full lines and their mean and dispersion are $\overline{P} = 1.04\%$ and $S_P = 1.26\%$, respectively. In Figure 7, the mean and the dispersion of the whole set of data ($N=11$) are $\overline{\theta} = 60^\circ.9$ and $S_\theta = 23^\circ.6$, respectively. Reliable data are shown with full lines ($N=6$) and their mean and dispersion are $\overline{\theta} = 60^\circ.7$ and $S_\theta = 26^\circ.8$, respectively.

2.2. NIR Data in the Direction of the BN region

2.2.1. Observations

Polarimetry on and around the BN object was done on 33 stars on 2002 February 15 (UT) using NSFCAM on the IRTF in polarimetry mode. The filter was the standard IRTF K -band filter centered on $\lambda = 2.2 \mu\text{m}$. A description of NSFCAM in polarimetry mode was given by Jones (1997). An identification number, J2000.0 coordinates, the degree of polarization, the position angle and their uncertainties are given in columns 1 to 6 in Table 5, respectively. Color indices $H - K$ are given in column 7. A precision of $\pm 0.3\%$ or better was reached for each observation and the relation, $\sigma_{\theta_K} = 28^\circ.6 / (P_K / \sigma_{P_K})$, was used with $\sigma_{P_K} = 0.3\%$, to estimate σ_θ in column 6. The optical depth τ_K at $\lambda = 2.2 \mu\text{m}$ was estimated for each of the 33 sources with equation (1) from Jones (1989) by using the relation $\tau_K = 1.5E_{H-K}$. The color excess was estimated by subtracting the intrinsic color index of middle M red dwarfs (Lada et al. 2004) $(H - K)_0 = 0.3$ from $H - K$ (column (7) of Table 5). Estimates of τ_K are displayed in column 12 of Table 5. The use of $(H - K)_0 = 0.3$ might introduce a bias in the results as one can see in Table 5 that negative values of optical depth are found for stars number 5 and 35. Since the median value of the distribution of $H - K$ is 0.83 we believe, however, that most of our estimates are good approximations of the optical depth.

Since coordinates of each object were defined relative to a zero coordinate origin during the observations, coordinates from BN and a value of $\approx 0''.9/\text{pixel}$ corresponding to the plate scale were used to compute the coordinates given in columns 2 and 3. A search for a possible identification of each object was then made by using the Simbad database. In many cases several objects are located a few arcseconds from these positions and each of the sources compiled in Table 5 can generally be identified as or associated to an IR source (IR), a Part of Cloud (PoC) source, a Maser (Mas), a Star in Cluster (*iC), a Star in Nebula (*iN), a Parenago object or a X-ray source (X). These possibilities are not all included in Table 5, but by comparisons with works by Lonsdale et al. (1982) (LBLS) and Stolovy et al. (1998), possible identifications for some of the sources are given in columns 8 to 10 in Table 5. Sources 18, 27 and 31 are suspected to be identified to objects named CB1, CB4 and n respectively

and discussed by Stolovy et al. (1998) and/or by Shuping et al. (2004) (S&S). CB1 and CB4 are Close Binaries while n is a point-like source and is believed to be surrounded by a circumstellar disk. Estimates of θ_{off} displayed in columns 11 will be introduced and discussed in the following sections.

Polarimetry on BN is consistent with $\lambda = 2.2 \mu\text{m}$ polarimetry by Lonsdale et al. (1980) and Minchin et al. (1991), and with $\lambda = 3.8 \mu\text{m}$ polarimetry by Dougados et al. (1993) on this source. However $\lambda = 2.2 \mu\text{m}$ polarimetry on source 31 (n) differs from $\lambda = 3.8 \mu\text{m}$ polarimetry by Dougados et al. (1993) on this source where $P \pm \sigma_P = 16.6 \pm 1.2\%$, $\theta \pm \sigma_\theta = 110 \pm 2^\circ$ with an angular resolution of $0''.8$, and where $P \pm \sigma_P = 12.6 \pm 4.0\%$, $\theta \pm \sigma_\theta = 115 \pm 8^\circ$ with an angular resolution of $0''.2$. A comparison with the $\lambda = 2.2 \mu\text{m}$ map by Minchin et al. (1991) shows that the polarization pattern shown in our map differs greatly from their centrosymmetric polarization vector pattern. Some of the vectors in our map appear sometimes to have a similar orientation to some vectors in their map but the comparison is difficult and limited without a tabulated version of their data. An outflow/disk system around BN was revealed with K -band high resolution observations by Jiang et al. (2005). In addition, $\lambda = 2.2 \mu\text{m}$ circular polarization of OMC-1 by Buschermöhle et al. (2005), wide-field and deep JHK_s -bands polarization images of the Orion Nebula by Tamura et al. (2006), HST NICMOS polarization measurements of OMC-1 at $\lambda = 2.2 \mu\text{m}$ with $0''.2$ resolution by Simpson et al. (2006), JHK_s -band polarimetry of ≈ 500 stars of the Orion Nebula Cluster in M42 by Kusakabe et al. (2008), and K_s -band circular and linear polarization by Fukue et al. (2009) are available on and around BN. A multi-data survey was conducted in OMC-1 by Vallée & Fiege (2007) and several configurations of magnetic fields are considered and discussed. The four possible mechanisms proposed for explaining circular polarization observed on large scale in OMC-1 are discussed and some of them investigated by Matsumura & Bastien (2009). Our data will be discussed and compared with some of these works.

2.2.2. Selection of the Data

The statistical behaviour of polarization efficiency at $2.2 \mu\text{m}$ has been explored by Jones (1989). A good correlation is found between interstellar extinction and interstellar polarization over a range in optical depth of a factor of 100. A least-squares fit to the sample of data obtained on 105 sources has a slope of 0.75 corresponding to the relation, $P_K = 2.23\tau_K^{3/4}$. The distribution of these data is shown with crosses in Figure 8 (see also Jones 1989). Except for stars number 5 and 35 toward which the estimates of τ_K are negative, the distribution of the new data set in OMC-1 is shown with diamonds, for comparison.

The upper solid line in Figure 8 corresponds to equation (A7) from Jones (1989), where $\eta = 0.875$ is used. With this choice of η , the solid line displayed in the Figure is equivalent to the one displayed in our Figure 1 and translates the relation $P_{\max} = 9.0E_{B-V}$ estimated by Serkowski et al. (1975).

We see that nine sources show a polarization degree higher than the upper limit. These stars are identified in the Figure and, in addition to sources 5 and 35, they are excluded from the analysis since their polarization could be contaminated by intrinsic polarization due to scattering as illustrated by Kusakabe et al. (2008) for some sources of their JHK_s -band polarization sample. The quality code SC associated to the rejected measurements is SC = 0. In a complementary way, the data located below the upper limit have a quality code SC = 1. The quality code is displayed in the last column of Table 5 where SC = 1 for reliable data and SC = 0 otherwise. Adding the set of twenty-two selected sources to the sample studied by Jones does not change the slope substantially. This can be seen in the Figure where the least squares-fit shown by the dashed line still has a slope of ≈ 0.75 , corresponding to the relation

$$P_K(\%) = 2.30\tau_K^{0.73}. \quad (1)$$

In other words the behavior of the polarization efficiency in OMC-1 is close to the statistical behavior observed toward various other LOSs in the Galaxy and the polarization efficiency, $P_K/\tau_K \propto \tau_K^{-1/4}$.

2.2.3. IR Polarization Map and Histograms of Polarization Data

All the data from Table 5 are shown in Figure 9. Data believed to be reliable to probe the magnetic fields are shown with solid polarization vectors while the other ones are shown with dashed polarization vectors. Histograms of polarization percentages and of polarization position angles of the reliable sample are shown in Figures 10 and 11, respectively. In Figure 10, the mean and the dispersion of the whole data set (N=22) are $\overline{P} = 4.89\%$ and $S_P = 5.47\%$, respectively. In Figure 11, the mean and the dispersion of the whole data set are $\overline{\theta} = 84^\circ.6$ and $S_\theta = 38^\circ.5$, respectively.

3. MULTI-SCALE ANALYSIS OF MAGNETIC FIELDS

In this section we compare magnetic fields probed at several wavelengths and on various spatial scales. All our basic statistical results are compiled in Tables 6 and 7. Each line shows means and dispersions for several regions. Since the foreground interstellar polarization in

this region was estimated by Bastien (1979) to be $P_{\text{IS}} = 0.53 \pm 0.15\%$ with $\theta_{\text{IS}} = 49^\circ \pm 8^\circ$, means and dispersions were systematically estimated for subsets of data with $P \geq 1\%$ and $P < 1\%$. In the following, except where explicitly mentionned, no foreground correction was applied to the data. A rotation of $\pm 90^\circ$ was applied to submm data to allow direct comparison with visible and NIR polarization position angles. All the $850 \mu\text{m}$ data have a signal-to-noise ratio such that $P/\sigma_P > 3$ (Poidevin et al. 2010). All the $350 \mu\text{m}$ data have a signal-to-noise ratio such that $P/\sigma_P > 2$ (Houde et al. 2004).

3.1. Comparison of Results on Large Spatial Scales in Orion A

All selected data from Tables 1, 2, 3 and 4 are shown in Figure 12 with all vectors drawn with the same length to get a clear picture of visible polarization position angles in Orion A. For this region, covering an area of $\approx 1.5^\circ \times 2^\circ$, we find a mean position angle of $\approx 89^\circ$ for the more highly polarized stars and a mean position angle of $\approx 67^\circ$ for those with a polarization $P \leq 1\%$ as displayed in column 3 of Table 6. See also histograms in Figures 4 and 7. Thus we confirm with a larger sample the results found by Breger (1976). He found a mean position angle of $\approx 100^\circ$ with high polarization stars, and a mean position angle of $\approx 75^\circ$ for low polarization stars, respectively. We point out that the mean position angle of $\approx 67^\circ$ obtained for stars with $P \leq 1\%$ is very close to the mean value of about 69° defined by Li et al. (2009) on an area of about $4^\circ \times 5^\circ$ (see their Figure 1) by using the catalog from Heiles (2000). Once the polarization results of all our data set have been corrected for the ISM polarization (Bastien 1979) we find a mean polarization angle of $\approx 104^\circ$ with a dispersion of $\approx 31^\circ$. When the same is done only on the stars with $P \geq 1\%$, we find a mean polarization angle of $\approx 99^\circ$ with a dispersion of $\approx 30^\circ$.

3.2. Comparisons on Various Scales Toward OMC-1

3.2.1. Comparison of Submm Data with Visible Data around OMC-1

Figure 13 shows visible data superimposed on the $350 \mu\text{m}$ data observed by Houde et al. (2004). All stars labeled in the Figure have reliable data according to our selection criteria $SC = 1$ or 2 . By referring to Tables 2 and 3, we see that polarization is produced by ICD grains and/or that these stars are located at distances greater than 500 pc from the Sun. By comparing the corresponding means and dispersions of the data set shown in Figure 13 and compiled in column 4 of Table 6, we see that apparently no spatial alignment on the POS exists between magnetic fields probed with both techniques. The mean visible polarization

position angle is $\approx 64^\circ$ with a dispersion of $\approx 39^\circ$ while once rotated by 90° the mean submm polarization position angle is at $\approx 112^\circ$ with a dispersion of $\approx 30^\circ$, making a mean offset of about 48° between the two mean uniform field components. We point out that these results are consistent with those found by Li et al. (2009) when visible polarization data are used on a larger scale.

3.2.2. Comparison of Submm Data with *K*-Band Data on and around BN

Figure 14 shows our $\lambda = 2.2 \mu\text{m}$ data superimposed on the $350 \mu\text{m}$ data observed by Houde et al. (2004). Here again, by comparing the corresponding means and dispersions of the data set shown in the figure and compiled in column 5 of Table 6, we find that apparently no spatial alignment on the POS exists between magnetic fields probed with both techniques. The mean *K*-band polarization position angle is $\approx 85^\circ$ with a dispersion of $\approx 39^\circ$ while once rotated by 90° the mean submm polarization position angle is at $\approx 120^\circ$ with a small dispersion of $\approx 9^\circ$, making a mean offset of about 35° between the two mean uniform field components. We point out, however, that a few stars, among which BN, show a polarization position angle consistent with the 90° rotated submm polarization angles in their neighborhood.

3.2.3. Comparison of *H*-Band Data with $350 \mu\text{m}$ and *K*-band Data

Wide-field ($\approx 8' \times 8'$) *JHK_s*-band polarimetry toward OMC-1 has been conducted by Kusakabe et al. (2008). Their Table 2 shows that the mean position angles obtained through each filter are consistent with the 90° rotated $350 \mu\text{m}$ mean polarization angles of Houde et al. (2004). We used the publicly available *H*-band data of Kusakabe et al. (2008) and find that apparently none of the stars observed at this wavelength matches the stars we observed in the *K*-band. The mean polarization position angle of the *H*-band data lying in the region shown in Figure 14 is $\approx 134^\circ$ with a dispersion of $\approx 27^\circ$.

3.2.4. A Rotating Magnetic Field on large scale toward OMC-1

The comparison of the means and dispersions discussed in the preceding subsections suggests that the geometry of the magnetic field toward OMC-1 could be relatively complex. This result is not a complete surprise since it has been known for a long time that a rotation occurs toward the LOS to BN and OMC-1/IRS2, two sources close to each other on the POS

(Lonsdale et al. 1980). Recent works, however, give clues to a possible rotation on a larger scale around BN and also toward OMC-1. Circular Polarization (CP) was obtained in the K_s -band by Fukue et al. (2009) on a region of $2'.7 \times 2'.7$ centered close to the position of BN. The authors find a good correlation between CP and extinction by using $H - K_s$ as a proxy for extinction. Their analysis also shows a good correlation between CP and linear polarization, and dichroic extinction would be the main mechanism producing the CP observed in this region. In addition, because of the well defined uniform submm polarization pattern, it seems reasonable to assume that turbulent effects can be neglected. This hypothesis is supported by the results of the angular dispersion analysis of the $350 \mu\text{m}$ polarization data of OMC-1 by Hildebrand et al. (2009) where the uniform magnetic field component on the POS is estimated to be ten times stronger than the turbulent magnetic field component in high density regions of the clouds.

In order to check the hypothesis of a rotation of the magnetic fields on a larger scale around BN and toward OMC-1 we have measured the offset in position angle between each K -band polarization vector and the 4 nearest submm polarization vectors located in their neighborhood (see Figure 14). Present grain alignment theory suggests that submm polarization vectors are perpendicular to the mean magnetic field direction on the POS, while visible polarization vectors should be parallel to this mean direction, so one would expect a spatial correlation between some components of the magnetic fields probed with both techniques. The histogram of the angular offset estimates is shown in Figure 15. We are concerned only with the magnitude of the difference between the visible and submm polarization vectors, therefore we convert all offsets to lie between 0° and 90° . If submm polarimetry probes mainly magnetic fields embedded into the clouds, a similar orientation of the fields probed at each wavelength would correspond to an angular offset of 90° . We find a peak around 70° suggesting that some stars observed in the K -band probe the same magnetic field component than submm data do. Other stars, however, show offsets between 0° and 50° implying that other magnetic field directions exist along LOSs toward OMC-1.

It was shown that NIR polarimetry at BN is dominated by dichroism and that the $\lambda = 2.2 \mu\text{m}$ degree of polarization and position angle are consistent with $100 \mu\text{m}$ data (see Lonsdale et al. 1980; Lee & Draine 1985; Jones 1989; Hough et al. 1996; Schleuning 1998; Jiang et al. 2005). In addition, in our sample BN has the second highest K -band polarization degree and the highest extinction parameter, therefore one would expect to see an increase of the degree of polarization, P_K , as well as an increase of the optical depth, τ_K , for angular offsets closer and closer to 90° . This result is suggested in Figure 16 with our relatively small sample of 22 measurements. The top part of Figure 16 shows values of P_K up to $\approx 20\%$ for angular offsets lying between $\approx 65^\circ$ and $\approx 90^\circ$ whereas values of $P_K \lesssim 5\%$ are found for angular offsets outside this range. The same trend is suggested in the bottom

part of Figure 16 where the highest values of τ_K are found for angular offsets around 90° whereas most of the values of τ_K lying between $\approx 0^\circ$ and $\approx 65^\circ$ are two to three times lower than those values.

As a further test of this idea, we used the larger H -band data sample of Kusakabe et al. (2008). Here again, we have measured the offset in position angle between each IR polarization vector and the 4 nearest submm polarization vectors located in their neighborhood. Because the $350\ \mu\text{m}$ data are gridded with $20''$ pixels we have restricted our calculations to distances smaller than $21''$ on the POS. This ensures that we avoid H -band data lying too far on the POS from the area mapped at $350\ \mu\text{m}$. The histogram of the angular offsets (top) and the distribution of P_H (middle) with those angular offsets are shown in Figure 17. An increase of the polarization degree, P_H , as a function of the angular offset can be seen in this figure. This result confirms the trend observed around BN with the smaller K -band data sample (Figure 15) and implies that the magnetic field could rotate from inside-out toward OMC-1 on a spatial scale larger than just the BN area of about $1'.5 \times 1'.5$. As a statistical check, we have calculated the mean polarization degrees in bins of 18° . The bottom part of Figure 17 shows a smooth increase of $\langle P_H \rangle$ from 2.5% to 7.0% for offsets increasing from $\approx 50^\circ$ to $\approx 80^\circ$. Within the uncertainties on the polarization position angles this trend is consistent with a rotation of the magnetic field of $\lesssim 60^\circ$ on large scale toward OMC-1. For angular offsets between 0° and 50° $\langle P_H \rangle$ is approximately constant at $\approx 2.5\%$ as illustrated by the horizontal dashed line.

3.3. Comparisons of Magnetic Fields in and around OMC-2 and OMC-3

The visible polarization data selected in Tables 1 to 4 are shown in Figures 18 and 19. They are superimposed on the $850\ \mu\text{m}$ polarization data observed and discussed by Poidevin et al. (2010). In the two maps all vectors are displayed with a similar size for a better visualization of the polarization position angles but two different size scales are used. Bold vectors show visible data and thin vectors show submm data.

Figure 18 shows the spatial distribution of the visible polarization vectors in and around OMC-2 and OMC-3 with respect to the polarization pattern produced by dust emission within the clouds. The means and dispersions relative to the two data sets shown in the Figure are given in column 3 in Table 7. Statistical values of the $350\ \mu\text{m}$ polarization data discussed by Houde et al. (2004) are also displayed in the Table. The two submm data sets show different means and dispersions. The mean orientation at $350\ \mu\text{m}$ is $\approx 45^\circ$ with a dispersion of $\approx 25^\circ$ while the $850\ \mu\text{m}$ data set has a mean of $\approx 56^\circ$ with a dispersion of $\approx 36^\circ$. Part of this difference is probably due to the smaller number of 350

μm measurements compared to the $850\ \mu\text{m}$ data set and to some differences in the regions covered by each map. For a detailed comparison between the two submm data sets see Poidevin et al. (2010). When looking from visible to submm data, the results show an anticlockwise rotation of $\approx 11^\circ$ and $\approx 22^\circ$ in the mean position angle when $850\ \mu\text{m}$ and $350\ \mu\text{m}$ data are considered, respectively. These results show good agreement between the mean orientation of the magnetic fields probed with both techniques in and around OMC-2/OMC-3.

Figure 19 shows a zoom on the two data sets displayed toward OMC-2. The means and dispersions for each subset of data shown in the Figure are compiled in column 4 in Table 7. The 90° -rotated mean polarization position angle of the $350\ \mu\text{m}$ pattern is found to be similar to the mean position angle of the visible data, $\approx 48^\circ$. However, the set of $850\ \mu\text{m}$ data gives a different mean position angle of $\approx 69^\circ$ with a large dispersion. These results suggest that magnetic fields probed with both techniques have a similar orientation projected on the POS, taking the small number of visible measurements ($N = 9$) into account.

Our results are generally consistent with those for OMC-2 and OMC-3 shown by Li et al. (2009) in their Table 1.

3.4. Comparisons of Magnetic Fields in and around OMC-4

Our results for this region are compiled in column 5 in Table 7. The mean polarization position angle of visible data covering the area shown in Figure 20 is $\approx 54^\circ$ with a dispersion $S_\theta \approx 36^\circ$. The 90° -rotated mean polarization position angle of the well defined $350\ \mu\text{m}$ polarization pattern is $\approx 76^\circ$ which yields a difference of $\approx 22^\circ$ between the magnetic field probed with visible and submm techniques on small scale around OMC-4. These values are consistent with the position angle of 69° for the ISM magnetic field on a larger scale inferred by Li et al. (2009).

4. DISCUSSION

The main trend of the comparative studies presented in section 3 is that magnetic fields probed with submm techniques inside the molecular star-forming ISF have directions generally consistent with those probed with visible techniques in the diffuse parts of the surrounding ISM, except for OMC-1 as discussed above in section 3.

For OMC-1, Schleuning (1998) compared the field lines probed with visible polarimetry data from Breger (1976) and Vrba et al. (1988) in the ambient envelope directly outside the

OMC-1 ridge with the field lines probed with 100 μm and 350 μm polarimetry data inside the clouds. He showed some similarity between the orientation of some components probed at each wavelength (as one can see also in our Figure 13). In addition the magnetic field component probed with IR polarimetry in the LOS to BN was found to be consistent with the one probed with submm data in the same LOS.

Our analysis presented in section 3.2 fills the gap between the two scales discussed by Schleuning (1998) and suggests that a large scale rotating magnetic field could be wrapping the OMC-1 clouds. The results suggest a rotation by $\lesssim 60^\circ$ toward OMC-1 (Figure 17). This is the first time that this trend has been shown with NIR data over such a wide field. This is also the first time that this twist has been shown to extend so deep into the cloud with linear polarimetry.

Based on a previous analysis by Martin (1974) and on large circular polarization measurements at $\lambda = 2.2 \mu\text{m}$ combined to linear polarimetry, Lonsdale et al. (1980) argued that the polarization of OMC-1/IRS1 (BN) and OMC-1/IRS2 is produced by a medium of aligned grains with a twist in the alignment $\lesssim 60^\circ$, providing support on a small scale to our analysis. More recent works by Hough et al. (1996) and by Aitken et al. (2006) also support this scenario along the LOS to BN. On a larger scale, based on the K -band and H -band coupled to submm data analysis shown in Figures 16 and 17, we think that the trend observed in those figures shows a rotation of the polarization plane toward OMC-1. Whether this rotation is produced by a two- or multi-slab model or by a spatially continuous rotation toward OMC-1 is not clear. Such possibilities were discussed by Aitken et al. (2006) and references therein. We now look at the 350 μm polarization pattern observed by Houde et al. (2004) and into the literature to find out if one scenario could prevail.

We divide the 350 μm polarization map into two main regions showing smooth polarization patterns with different mean orientations. The first region is located in the south-western part of the map where $\delta \lesssim -5^\circ 24'$ (see Fig. 13). Most if not all the 350 μm data in this region show a polarization position angle $\theta > 90^\circ$. This distribution yields a mean magnetic field direction of $\overline{\theta_B} \approx 60^\circ$. Interestingly, this mean orientation is close to the one found with visible data in the vicinity of OMC-1 (see column 4 of Table 6) along LOSs of small visual extinction. For this reason, in the following we call this region of the cloud the near region. Going north-east of this region, the polarization falls to zero, and then the position angles turn by an angle $\approx 90^\circ$. Beyond the strip of (almost) null vectors, mainly in the northern part of the map, most of the 350 μm vectors have a polarization position angle such that $\theta < 90^\circ$. Those data yield a mean magnetic field orientation $\overline{\theta_B} \approx 123^\circ$. This component would be mostly background to the cloud, in agreement with the NIR position angle observed on BN (see Fig. 14). In the following we call this region the far region.

In Figure 4 of Kusakabe et al. (2008), where $\delta > -05^{\circ}23'$, most of their blue vectors match well with the far region, some of them showing high polarization values. South of this declination, the IR polarization vectors matching well the far region are those showing a ‘small’ polarization degree of 1-3%. Such a low polarization could be explained by superposition of the near region mean field component at $\overline{\theta_B} \approx 60^{\circ}$ but dominated by the far region field component along these LOSs. This decrease of polarization is supported by our angular offsets analysis displayed in Figure 17. Kusakabe et al. (2008) suspect multiple field components in this region, known as the bar, and due to a photodissociation front. Houde et al. (2004) found an inclination of 49° for the magnetic field near the bar with respect to the LOS, which would also contribute to a lower polarization.

The separation of the submm polarization pattern into two regions discussed above suggests the existence of at least two slabs of aligned dust grains toward OMC-1. If these slabs extend all over OMC-1 one expects to observe Circular Polarization (CP) produced mainly by birefringence as well as Linear Polarization (LP) produced by dichroic absorption (e.g. Martin 1974). The HST NICMOS polarization measurements of OMC-1 at $\lambda = 2.0 \mu\text{m}$ with $0.2''$ resolution by Simpson et al. (2006) and covering $\approx 20'' \times 40''$ on and around BN show that although polarization produced by scattering is present around several sources, a component produced by dichroic extinction appears to dominate through several lines of sight. On a slightly larger scale Fukue et al. (2009) searched for a correlation between CP and LP on a region covering $\approx 2'.5 \times 2'.5$ centered around BN. Their observations show a good correlation between the degree of LP in the K_s band and $H - K_s$ used as a proxy for extinction. Their study also shows a correlation between the degree of CP and the degree of LP oriented at $\pm 45^{\circ}$ relative to the grain alignment axis but a lack of correlation between CP and LP parallel or perpendicular to the grain axis which is indicative that CP is mainly produced by birefringence. On a larger scale in OMC-1, Buschermöhle et al. (2005) show that the degree of CP correlates with reddening in the molecular cloud, as measured by the $J - K$ color index. CP appears to be generally very low toward less dense regions dominated by H_{II} , in agreement with the correlations found by Fukue et al. (2009).

We suspect that the zone where the $350 \mu\text{m}$ polarization is almost null corresponds to LOSs where the effects of the two large scale components cancel mutually. Such an effect where two regions have a different grain alignment along the LOS is expected to give rise to circular polarization. This is confirmed by the CP map of Buschermöhle et al. (2005) in their figure 3 where one can see knots of high CP in various locations along the strip which corresponds to null submm polarization. The area covered by their Figure 3 is shown by the blue rectangle in our Figure 13. The end of the strip where the submm polarization is null is located in the lower left corner of that blue box. On the contrary, two regions of higher CP showing higher submm LP are seen in the upper part of the Figure. One of those was

observed by Chrysostomou et al. (2000) (see also Figure 1 of Buscherhöhle et al. 2005). In this region Matsumura & Bastien (2009) show that the high degree of CP could be explained by scattering of highly linearly polarized incident light.

The schematic model that emerges is shown in Fig. 21. The 850 μm map of Johnstone & Bally (1999) is used to show the ISF. The symmetry axis of the two large scale magnetic field components seen in the 350 μm data is suggested by the vertical translucent line. The morphology of the large scale magnetic field pervading OMC-1 is shown by the large scale two component structure. The foreground component is shown with a full line while the background component is shown with a dashed line. The drawn by eye green-blue vectors show the mean orientation of the magnetic field probed by submm data in several subregions. The black circles indicate regions where the foreground and background magnetic field components probably cancel each other within OMC-1. The crosses (right) and head arrows (left) indicate the direction of the magnetic field with respect to the LOS as suggested by Zeeman measurements (see Fig. 15 in Heiles 1997). Crosses indicate magnetic fields pointing away from the observer and head arrows magnetic fields pointing toward the observer. The rotation that is produced when moving from the far region, i.e. OMC-1, toward us on the LOS is illustrated by the blue arrows. The sense of the rotation is based on the combination of the two following assumptions. The twist of the magnetic field along the LOS to BN of $\lesssim 60^\circ$ (Martin 1974; Lonsdale et al. 1980) is indicative of the amount of rotation over the whole OMC-1 region. The vectors shown in Figure 14 with a polarization degree of a few percent (e.g. sources 13, 15, 21) are associated to the near region while those showing high polarization degree (e.g. sources 8, 20, BN) are associated to the far region. Combining all the preceeding information the large scale magnetic field wrapping OMC-1 should be oriented from north to south. It is illustrated by the arrows on the solid and dashed lines. Such an orientation would be consistent with a reversal of the field lines direction toward OMC-1 as suggested by Zeeman measurements, and with the rotation of the magnetic field by $\lesssim 60^\circ$ toward OMC-1.

This two-component magnetic field model is not perfect but it does explain a significant fraction of our data. Such a large scale magnetic field pattern is compatible with the results of Hildebrand et al. (2009) that uniform magnetic field components dominate over turbulent components within OMC-1. Such a large scale structure is also in agreement with the statistical analysis of Li et al. (2009) on 25 molecular clouds which shows a significant correlation between the giant molecular clouds accumulation scale and the cloud cores scale. A comparison of their results with simulations favors sub-Alfvénic cases where magnetic fields play a significant role.

There is a significant possibility that this two-component model extends to the north

beyond the OMC-1 region. Matthews et al. (2001) interpreted their OMC-3 submm data in terms of a helical field. Poidevin et al. (2010) showed that the uniform magnetic field component is dominant in OMC-3, and comparable to the turbulent component in OMC-2. It will be very interesting to find out if these results are confirmed by upcoming future observations with POL-2 and SCUBA-2 at the JCMT.

5. SUMMARY

Polarimetry in a broad red bandpass on 69 stars, 41 of which had never been observed polarimetrically before, was combined with polarimetry in the V , R and I bands on 14 stars through and around OMC-2, and with K -band polarimetry on 33 stars through OMC-1. Together with published measurements, these measurements led to a representation of the morphology of magnetic fields through and around the filaments and star forming regions OMC-1, OMC-2, OMC-3 and OMC-4 in Orion A. Our main conclusions are summarized as follows.

1. Magnetic fields probed inside OMC-2, OMC-3 and OMC-4 in the submm are generally consistent with those probed in the diffuse parts of the ISM in the surroundings of Orion A with visible polarimetry. Li et al. (2009) conducted the same analysis at scales lying between the accumulation scale length and the size of cloud cores. They found a significant correlation for field directions detected from the two extremes. Our analysis confirms their results on intermediate scales.

2. In OMC-1, we measured the angular offsets between the K -band and the $350\ \mu\text{m}$ polarization data. We find high values of the polarization degree, P_K , and the optical depth, τ_K , close to angular offsets of 90° whereas lower values of P_K and τ_K are observed for smaller offsets. On a larger scale, we measured the distribution of angular offsets between available H -band polarization data and the same submm data set. Here we find an increase of $\langle P_H \rangle$ with angular offset which we interpret as a rotation of the magnetic field by $\lesssim 60^\circ$. These trends generalize results that were known only toward the LOSs to BN and OMC-1/IRS2 (e.g., Lonsdale et al. 1980; Hough et al. 1996; Aitken et al. 2006) and are consistent with a twist of the magnetic field on a larger scale toward OMC-1.

3. A comparison of our results with several other studies suggests that a two-component magnetic field or an helical magnetic field could be wrapping the OMC-1 filament, as illustrated in Fig. 21. The background component is oriented mostly at $\overline{\theta_B} \approx 120^\circ$ on the POS, and the foreground component is oriented mostly at $\overline{\theta_B} \approx 60^\circ$. This magnetic field model is compatible with the direction of the field along the LOS determined from Zeeman measure-

ments around Orion A (Heiles 1997). It is also coherent with the fact that uniform magnetic field components dominate over turbulent components in OMC-1 (Hildebrand et al. 2009) and that an external field could be wrapping the OMC-1 filament (Vallée & Fiege 2007).

This research is supported by the Conseil de recherche en sciences naturelles et en génie du Canada. FP thanks the Fundação de Amparo à Pesquisa do Estado de São Paulo (FAPESP grant number 2007/56302-4) for its support during the second phase of the present research. The authors thank B. Malenfant and G. Turcotte for their helpful and friendly support during observations at Mont-Mégantic Observatory. This work made use of the SIMBAD database at the Canadian Astronomy Data Center, which is operated by the Dominion Astrophysical Observatory for the National Research Council’s Herzberg Institute of Astrophysics.

REFERENCES

- Aitken, D.K., Hough, J.H. & Chrysostomou, A. 2006, MNRAS 366, 491
- Bastien, P. 1979, Polarization of T Tauri Stars, Ph.D. Thesis, University of Western Ontario.
- Breger, M. 1977, ApJ, 215, 119
- Breger, M. 1976, ApJ, 204, 789
- Brown, A.G.A., de Geus, E.J. & de Zeeuw, P.T. 1994, A&A, 289, 101
- Buschermöhle, M.; Whittet, D. C. B.; Chrysostomou, A.; Hough, J. H.; Lucas, P. W.; Adamson, A. J.; Whitney, B. A. & Wolff, M. J. 2005, ApJ, 624, 82
- Castets, A. & Langer, W.D. 1995, A&A, 294, 835
- Chini, R., Reipurth, B., Ward-Thompson, D., Bally, J., Nyman, L.-Å., Sievers, A., & Billawala, Y. 1997, ApJ, 474, L135
- Chrysostomou, A., Gledhill, T.M., Ménard, F., Hough, J.H., Tamura, M. & Bailey, J. 2000, MNRAS 312, 103
- Cudlip, W., Fruniss, I., King, K.J. & Jennings, R.E. 1982, MNRAS, 200, 1169
- Dobashi, K., Uehara, H., Kandori, R., Sakurai, T., Kaiden, M., Umemoto, T. & Sato, F. 2005, PASJ, 57S, 1
- Dougados, C., Léna, P., Ridgway, S.T., Christou, J.C. & Probst, R.G. 1993, ApJ, 406, 112
- Ducati, J.R., Ribeiro, D. & Rembold, S.B. 2003, ApJ, 588, 344
- Fukue, T., Tamura, M., Kandori, R., Kusakabe, N., Hough, J., Lucas, P.W., Bailey, J., Whittet, D.C.B., Nakajima, Y., Hashimoto, J. & Nagat, T. 2009, ApJ, 692, L88
- Hall, J.S. & Mikesell, A.H. 1949, AJ, 54, 187
- Heiles, C. 2000, ApJ, 604, 923
- Heiles, C. 1997, ApJSS, 111, 245
- Hildebrand, R.H., Dragovan, M. & Novak, G. 1984, ApJ, 284, L51
- Hildebrand, R.H., Kirby, L., Dotson, J.L., Houde, M., & Vaillancourt, J. 2009, ApJ, 696, 567

- Hiltner, W.A. 1949, ApJ, 109, 471
- Houde, M., Dowell, C.D., Hildebrand, R.H., Dotson, J.L., Vaillancourt, J.E., Phillips, T.G., Peng, R. & Bastien, P. 2004, ApJ, 604, 717
- Hough, J.H., Chrysostomou, A., Messinger, D.W., Whittet, D.C.B., Aitken, D.K. & Roche, P.F. 1996, ApJ, 461, 902
- Jiang, Z., Tamura, M., Fukagawa, M., Hough, J., Lucas, P. Suto, H., Ishii, M. & Yang, J. 2005, Nature, Vol. 437
- Jones, T. J. 1997, AJ, 114, 1393
- Jones, T.J., Mergen, J., Odewhan, S., Gehrz, R.D., Gatley, I., Merrill, K.M., Probst, R. & Woodward, C.E. 1994, AJ, 107, 2120
- Jones, T.J. 1989, ApJ, 346, 728
- Johnstone, D. & Bally, J. 1999, ApJ, 510, L49
- Kusakabe, N., Tamura, M., Kandori, R., Hashimoto, J., Nakajima, Y., Nagata, T., Nagayama, T., Hough, J. & Lucas, P. 2008, AJ, 136, 621
- Lada, C.J., Muench, A.A., Lada, E.A. & Alves, J.F. 2004, AJ, 128, 1254.
- Lazarian, A. 2003, JQSRT, 79-80, 881-902
- Lazarian, A. 2007, JQSRT, 1-3, 225-256
- Lee, H.M. & Draine, B.T. 1985, ApJ, 290, 211
- Li, H.-B., Dowell, D.C., Goodman, A., Hildebrand, R. and Novak, G. 2009, ApJ, 704, 891
- Lonsdale, C.J., Becklin, E.E., Lee, T.J. & Stewart, J.M. 1982, AJ, 87, 12.
- Lonsdale, C.J., Dyck, H.M., Capps, R.W. & Wolstencroft, R.D. 1980, ApJ, 238, L31
- Manset, N. & Bastien, P. 1995, PASP, 107, 483
- Martin, P.G. 1974, ApJ, 187, 461
- Mathewson, D.S. & Ford, V.L. 1970, MNRAS, 74, 139
- Matthews, B.C., & Wilson, C.D. 2000, ApJ, 531, 868
- Matthews, B.C., Wilson, C.D., & Fiege, J.D. 2001, ApJ, 562, 400

- Matsumura, M. & Bastien, P. 2009, *ApJ*, 697, 807
- Menten, K.M., Reid, M.J., Forbrich, J. & Brunthaler, A. 2007, *A&A*, 474, 515
- Minchin, N.R., Hough, J.H., McCall, A., Burton, M.G., McCaughrean, M.J., Aspin, C., Bailey, J.A., Axon, D.J. & Sato, S. 1991, *MNRAS*, 248, 715
- Poidevin, F. & Bastien, P. 2006, *ApJ*, 650, 945
- Poidevin, F. & Bastien, P., Matthews, B. 2010, *ApJ*, 716, 893
- Schleuning, D. A. 1998, *ApJ*, 493, 811
- Serkowski, K., Mathewson, D.S. & Ford, V.L. 1975, *ApJ*, 196, 261.
- Shuping, R.Y., Morris, M. & Bally, J. 2004, *AJ*, 128, 363
- Simpson, J.P., Colgan, S.W.J., Erickson, E.F., Burton, M.G. & Schultz, A.S.B. 2006, *ApJ*, 642, 339-353
- Sitko, M. L., Schmidt, G. D., & Stein, W. A. 1985, *ApJS*, 59, 323
- Stolovy, S.R., Burton, M.G., Erickson, E.F., Kaufman, M.J., Chrysostomou, A., Young, E.T., Colgan, S.W. J., Axon, D. J., Thompson, R.I., Rieke, M.J. & Schneider, G. 1998, *ApJ*, 492, L151
- Tamura, M., Kandori, R., Kusakabe, N., Nakajima, Y., Hashimoto, J., Nagashima, C., Nagata, T., Nagayama, T., Kimura, H. & Yamamoto, T. 2006, *ApJ*, 649, L29
- Vallée, J.P. & Fiege, J.D. 2007, *AJ*, 133, 1012
- Vrba, F.J., Strom, S.E. & Strom, K.M. 1988, *AJ*, 96, 680
- Wardle, J.F.C., & Kronberg, P.P. 1974, *ApJ*, 194, 249

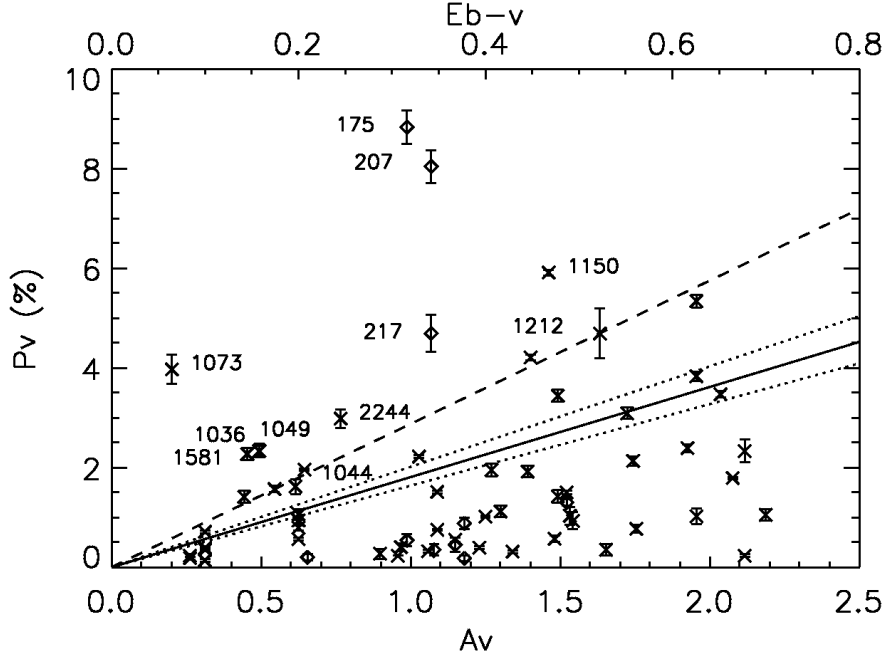


Fig. 1.— Variations of P with A_V . Upper axis shows $E_{B-V} = A_V/3.1$ for comparison. The mean of selective to total extinction ratios $\overline{R} = 4.93 \pm 0.51$ from Ducati et al. (2003) is used. The solid line shows the limit $P = 9E_{B-V}$ when parameter $\overline{R} = 4.93$ is used. Dotted lines show the corresponding limits covered by this relation when uncertainties on \overline{R} are included. The dashed line shows the same limit when the usual value of $\overline{R} = 3.10$ is considered. The reliability of the data refers to their reliability to probe magnetic fields (see section 2.1.3 for details). Crosses show reliable and less reliable data from Tables 1, 2 and 3. Diamonds also show reliable and less reliable data from Table 4 where the R -band is used.

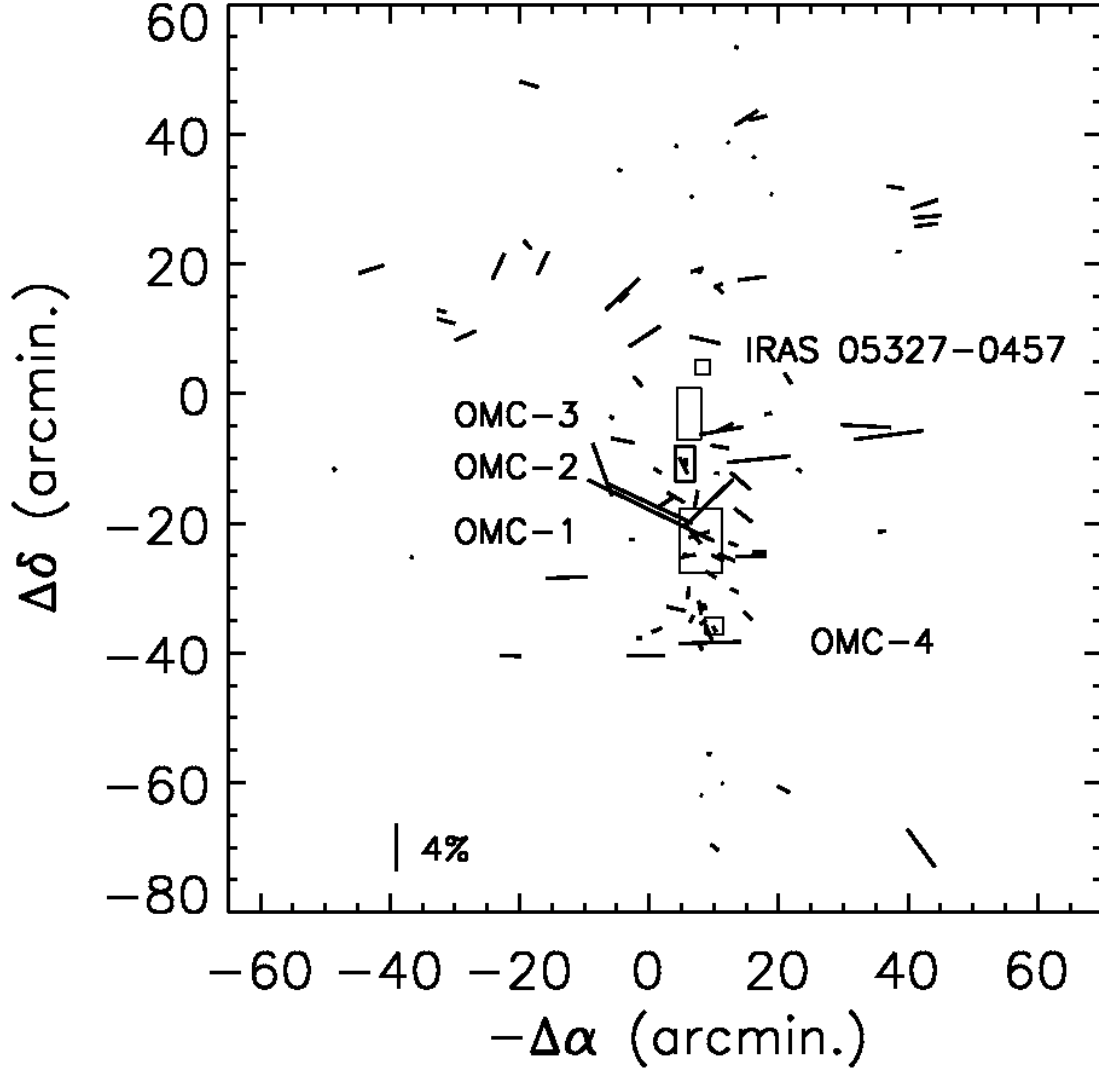


Fig. 2.— Visible polarization map of Orion A. The reliability of the data refers to their reliability to probe magnetic fields (see section 2.1.3 and 2.1.4 for details). Reliable data labeled with ‘1’ or ‘2’ and less reliable data labeled with ‘?’ from Tables 1, 2 and 3 are shown in the Figure. Five different regions identified by boxes are labeled. The reference position is R.A.=5^h35^m48.0^s, decl.=−5° 00^{mn} 00.0^s (J2000.0). See Figure 12 for a better polarization position angle visualization.

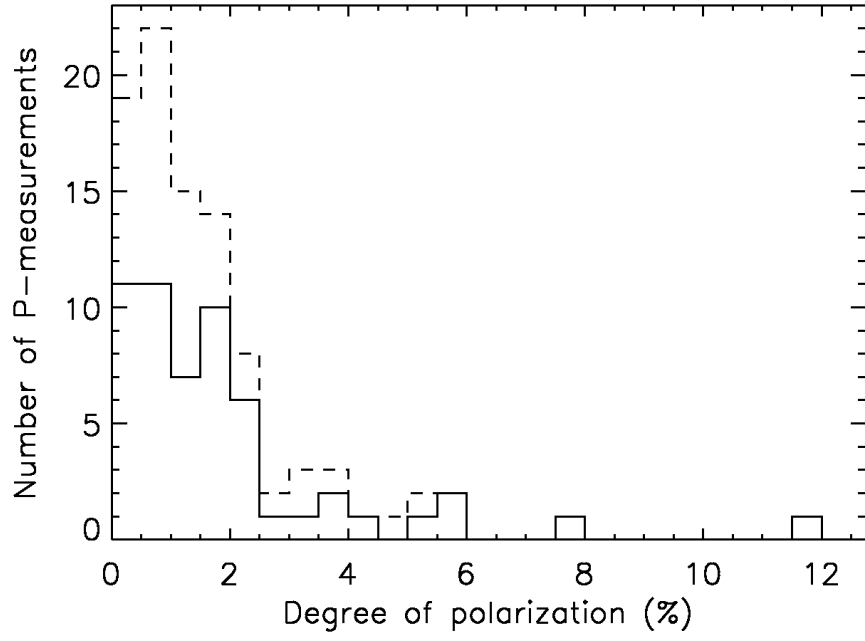


Fig. 3.— Histogram of the degree of polarization of visible data from Tables 1, 2 and 3 shown in Figure 2. Data considered as reliable data to probe magnetic fields ($SC = 1$ or 2) are shown with full lines. Less reliable data ($SC = ?$) are shown with dashed lines.

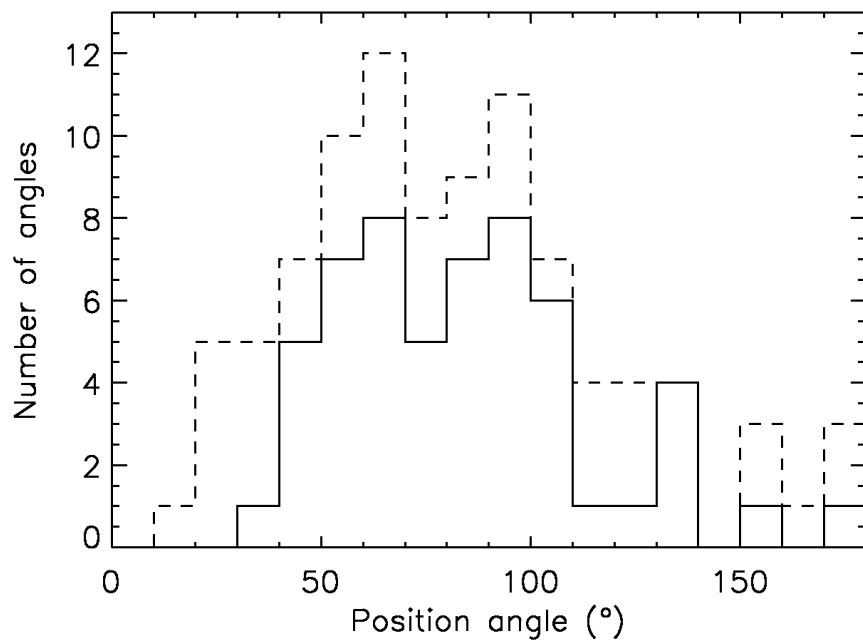


Fig. 4.— Same as in Figure 3 but for position angles.

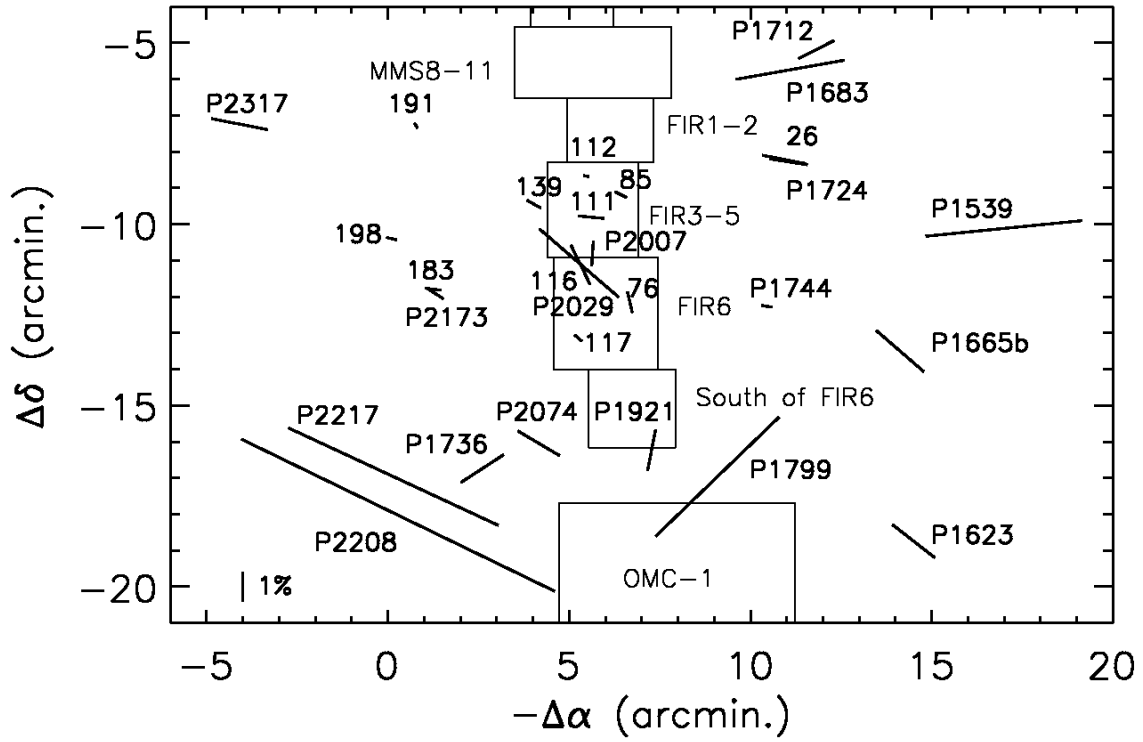


Fig. 5.— Same as in Figure 2 but with a zoom on OMC-2. Selected *R*-band data from Table 4 are now included. Subregions of OMC-2, FIR1-2, FIR3-5, FIR6, and south of FIR6 are indicated by boxes. The reference position is R.A.=5^h35^m48.0^s, decl.=−5° 00^{mn} 00.0^s (J2000.0).

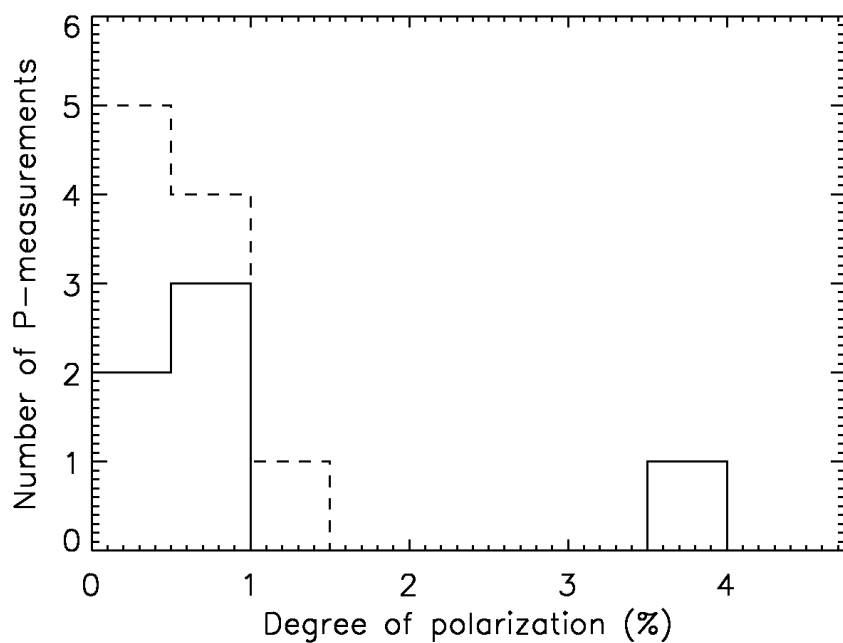


Fig. 6.— Histogram of the degree of polarization of the selected *R*-band data from Table 4 shown in Figure 5. Data considered as reliable data to probe magnetic fields ($SC = 1$ or 2) are shown with full lines. Less reliable data ($SC = ?$) are shown with dashed lines.

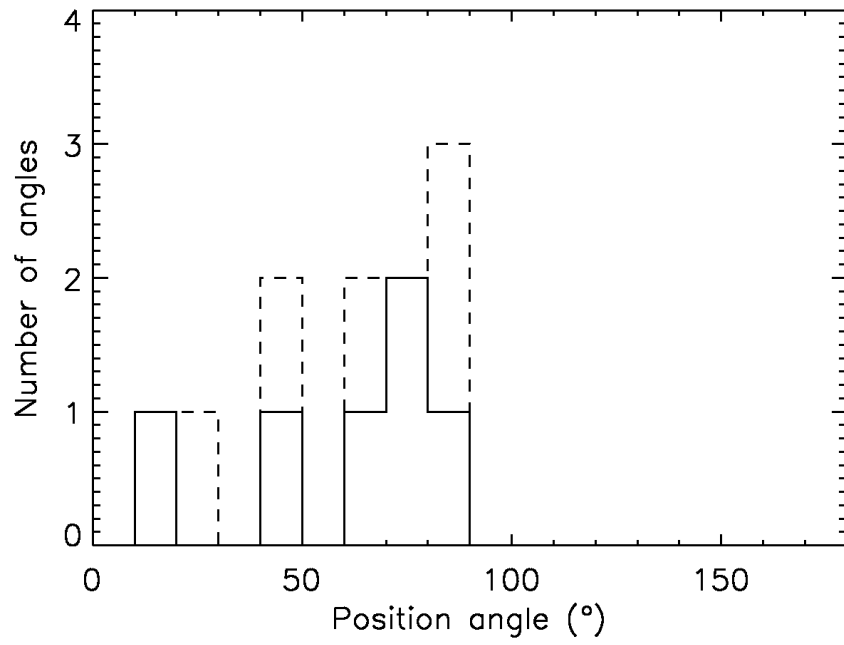


Fig. 7.— Same as in Figure 6 but for position angles.

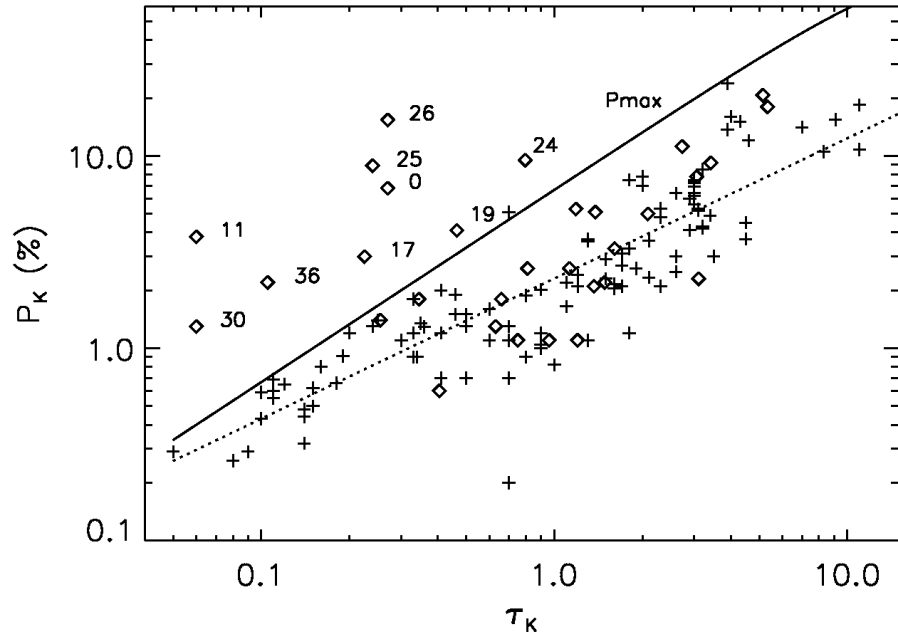


Fig. 8.— Variations of P_K with τ_K . Crosses show the distribution of the data discussed by Jones (1989). Diamonds show the distribution of the new data obtained in OMC-1. The dashed line shows the fit to all the data shown in the Figure once those lying above the P_{\max} line are removed from the sample (see text for details).

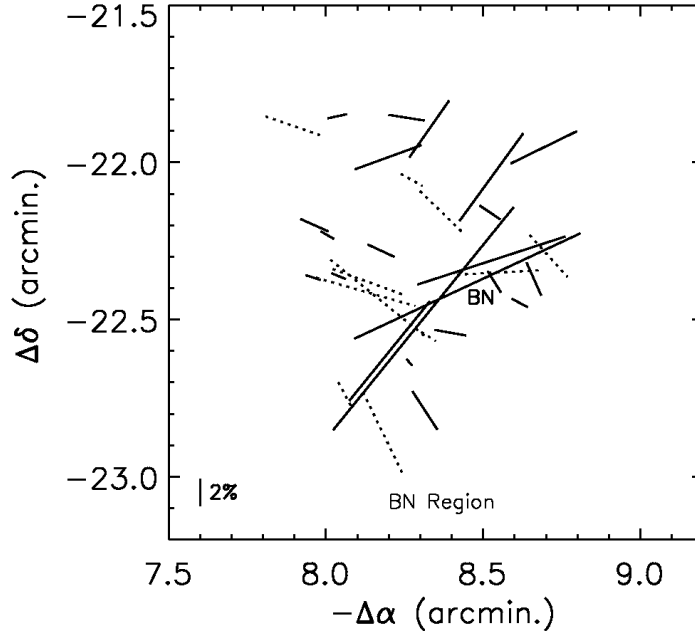


Fig. 9.— K -band polarization map in the region of the BN object. Data are from Table 5. Solid vectors show reliable data probing the fields while other data are shown with dashed vectors. The reference position is R.A.= $5^{\text{h}}35^{\text{m}}48.0^{\text{s}}$, decl.= $-5^{\circ}00^{\text{m}}00.0^{\text{s}}$ (J2000.0).

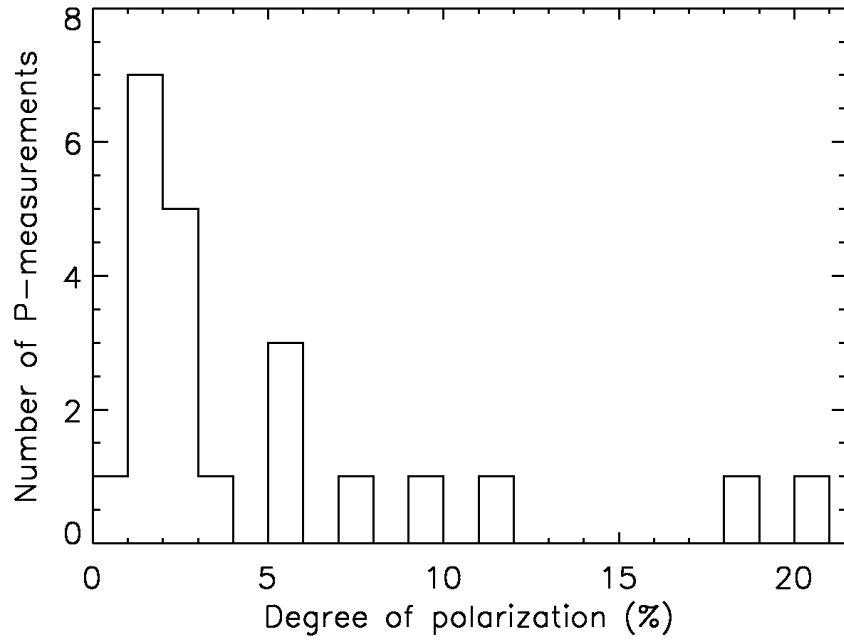


Fig. 10.— Histogram of the K -band degrees of polarization in the BN region. See Figure 9 and Table 5. Only reliable data are shown. Five stars show a polarization degree $> 6\%$.

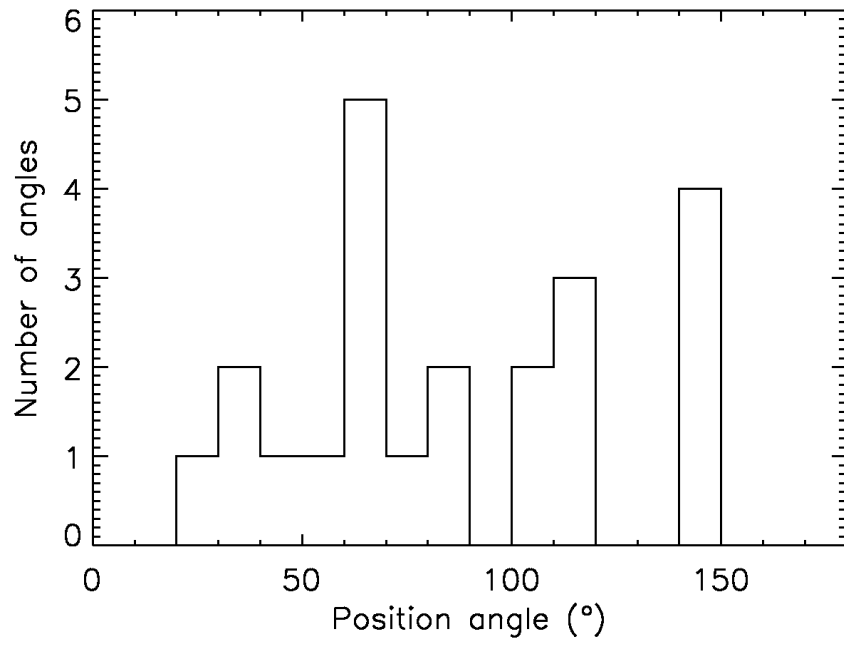


Fig. 11.— Same as in Figure 10 but for position angles.

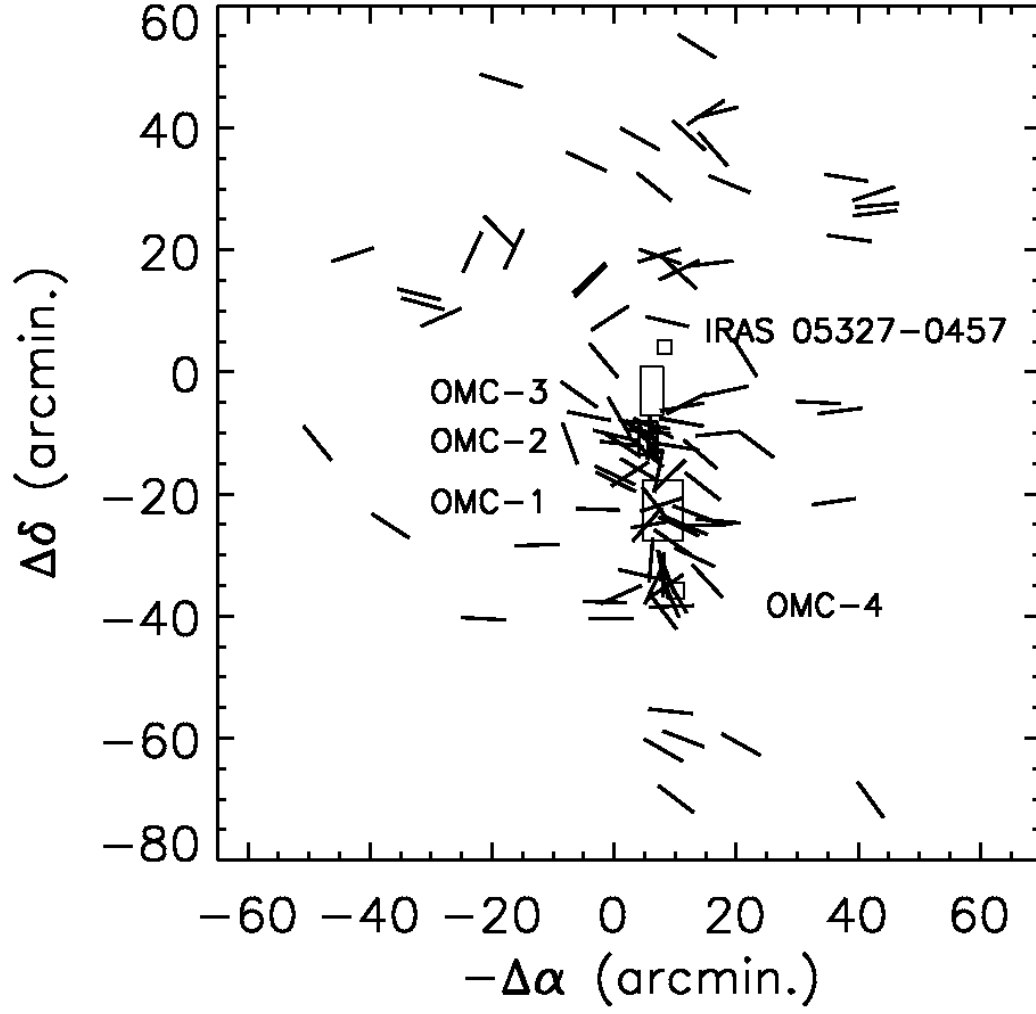


Fig. 12.— Same as in Figure 2 but now all vectors have the same length for better visualization of the polarization position angles.

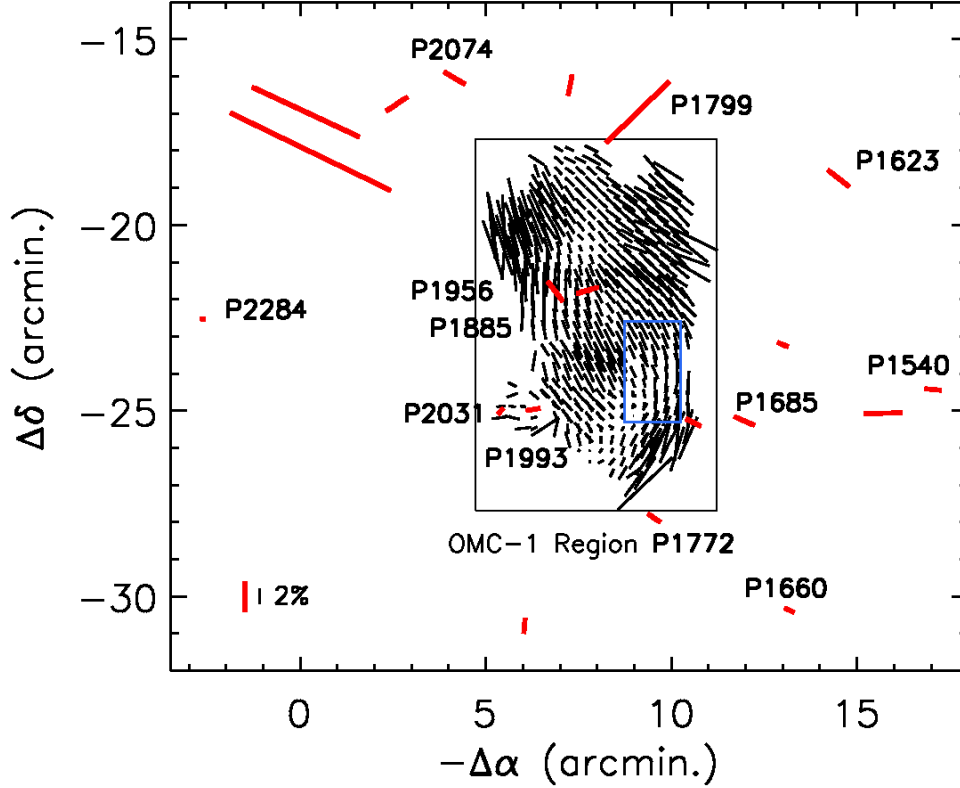


Fig. 13.— Visible and $350\ \mu\text{m}$ polarization map of OMC-1. The black rectangle delineates OMC-1. Submm data traced with thin vectors are from Houde et al. (2004). The reliability of the data refers to their reliability to probe magnetic fields (see section 2.1.3 and 2.1.4 for details). Named stars have reliable data according to this definition. The red vector located close to the middle of the submm map refers to star P1885. The blue rectangle shows the SW region observed by Buschermöhle et al. (2005) (see discussion for details). The reference position is R.A.= $5^{\text{h}}35^{\text{m}}48.0^{\text{s}}$, decl.= $-5^{\circ}00^{\text{m}}00.0^{\text{s}}$ (J2000.0).

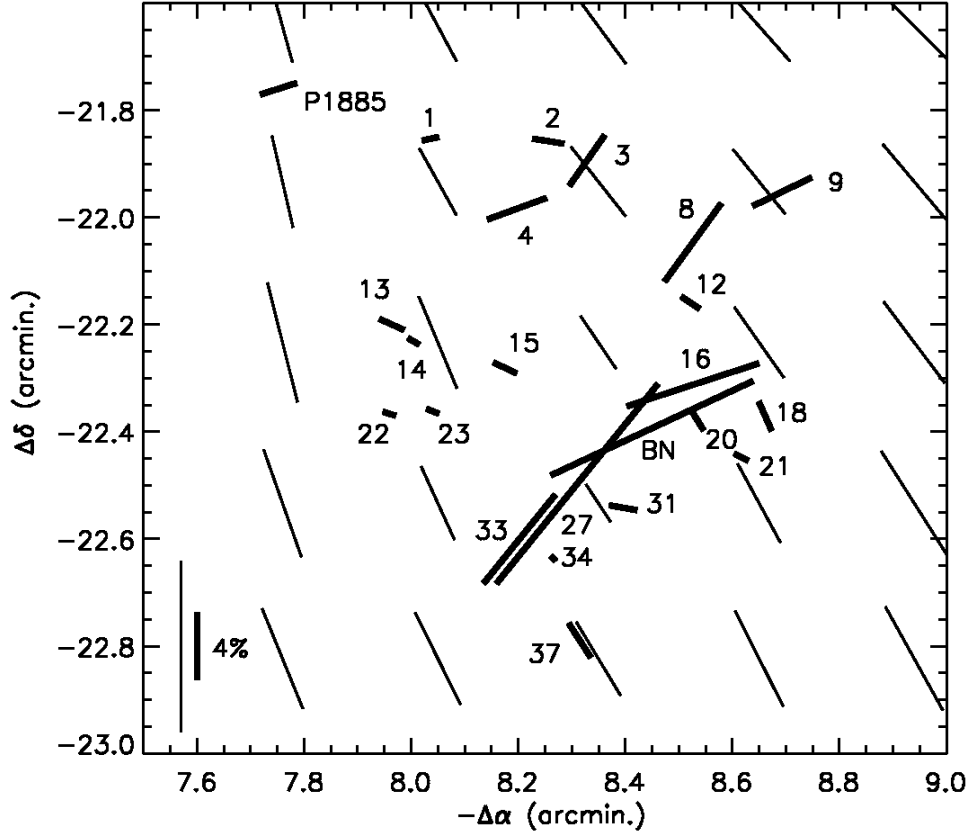


Fig. 14.— IR ($\lambda = 2.2 \mu\text{m}$) and submm ($\lambda = 350 \mu\text{m}$) polarization map through the BN region. Submm data are from Houde et al. (2004). Selected K -band data from Table 5 are shown with bold lines. Also shown in the map is the visible measurement on P1885 from Table 2. Submm data are shown with thin lines. Both scales are given at the bottom left in the Figure. This map can be compared with the one shown in Figure 9. BN is located at $(\alpha(2000), \delta(2000)) = (5:35:14.2, -5:22:23.6) = (-8.45', -22.39')$. The reference position is R.A. = $5^{\text{h}}35^{\text{m}}48.0^{\text{s}}$, decl. = $-5^{\circ}00^{\text{m}}00.0^{\text{s}}$ (J2000.0).

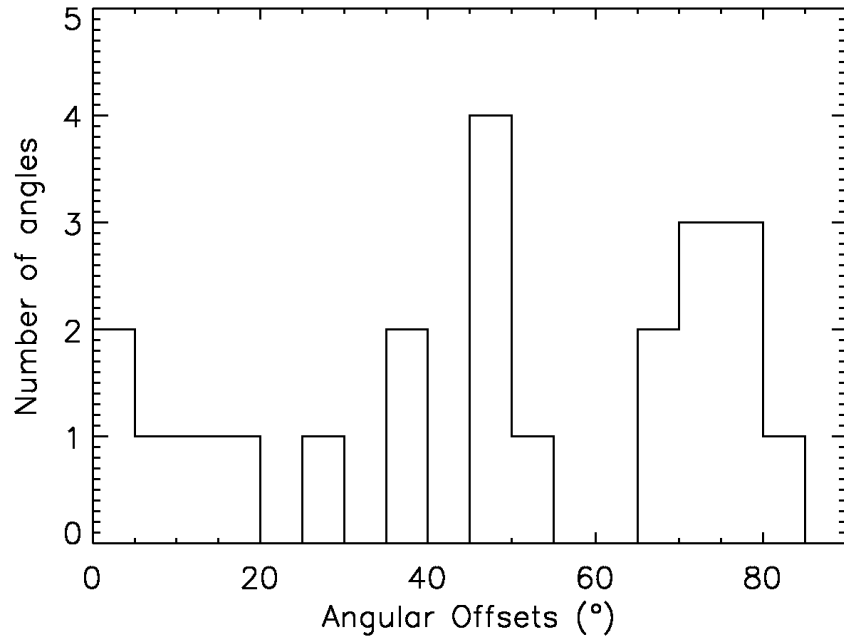


Fig. 15.— Histogram of the mean offsets of polarization position angles between $2.2\ \mu\text{m}$ and $350\ \mu\text{m}$ data shown in Figure 14.

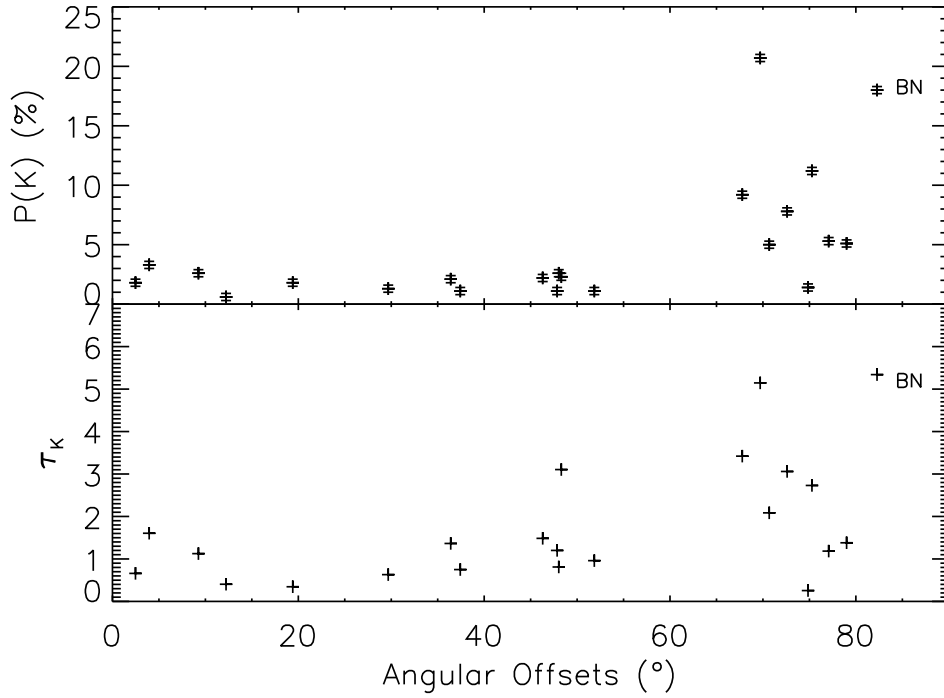


Fig. 16.— P_K versus θ_{off} (top) and τ_K versus θ_{off} (bottom) for sources selected in Table 5 and shown in Figure 14. We find an increase of both the degree of polarization, P_K , and the optical depth, τ_K , for angular offsets around 90° , indicative of a rotation of the magnetic field toward LOSs to BN and its vicinity.

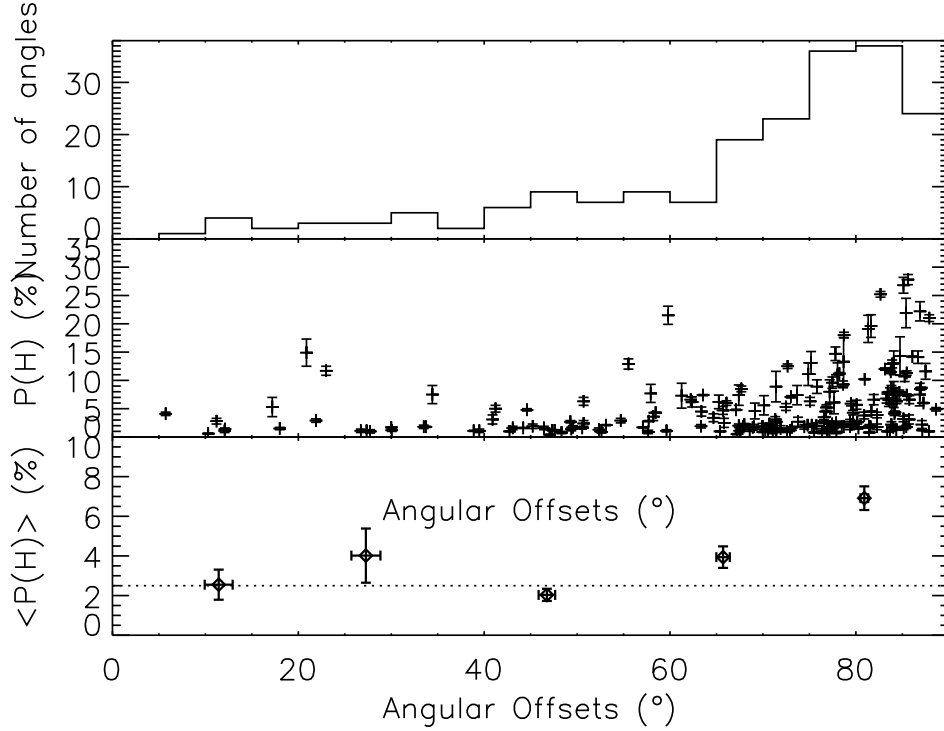


Fig. 17.— Histogram of the angular offsets between H -band polarization data from Kusakabe et al. (2008) and $350\ \mu\text{m}$ data from Houde et al. (2004) (top), the distribution of P_H with these angular offsets (middle) and the distribution of $\langle P_H \rangle$ with mean angular offsets in bins of 18° (bottom). All selected H -band data have a polarization percentage and uncertainty such that $P/\sigma_P > 3$. $\langle P_H \rangle$ increases as a function of the angular offsets between $\approx 50^\circ$ and $\approx 90^\circ$, and $\langle P_H \rangle \approx 2.5\%$ outside this range (horizontal dashed line).

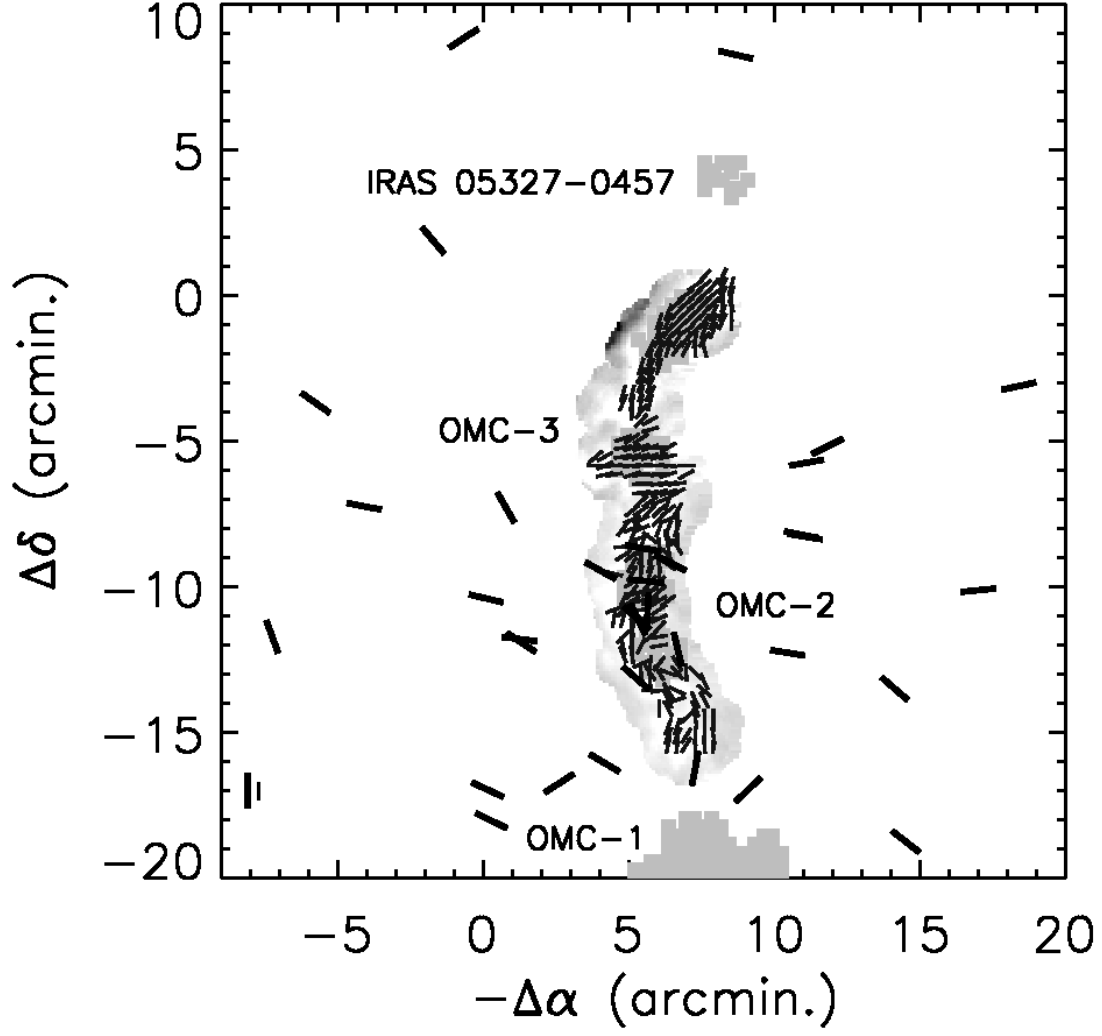


Fig. 18.— A map of $850\ \mu\text{m}$ data (Poidevin et al. 2010) superimposed on visible data. Vectors in each wavelength regime have the same length for better visualization of the polarization position angles, with the scales given in the bottom left. Bold vectors: visible data. Thin vectors: submm data. The reference position is R.A.= $5^{\text{h}}35^{\text{m}}48.0^{\text{s}}$, decl.= $-5^{\circ}00^{\text{m}}00.0^{\text{s}}$ (J2000.0).

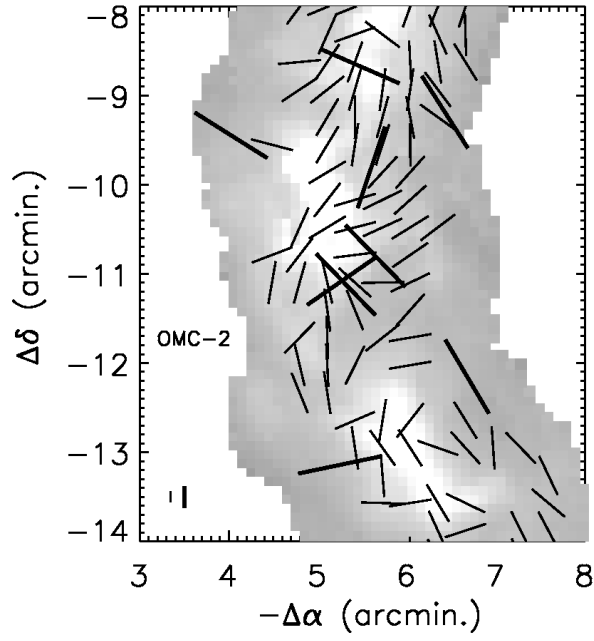


Fig. 19.— Same as in figure 18 but with a zoom on regions FIR3 to FIR6.

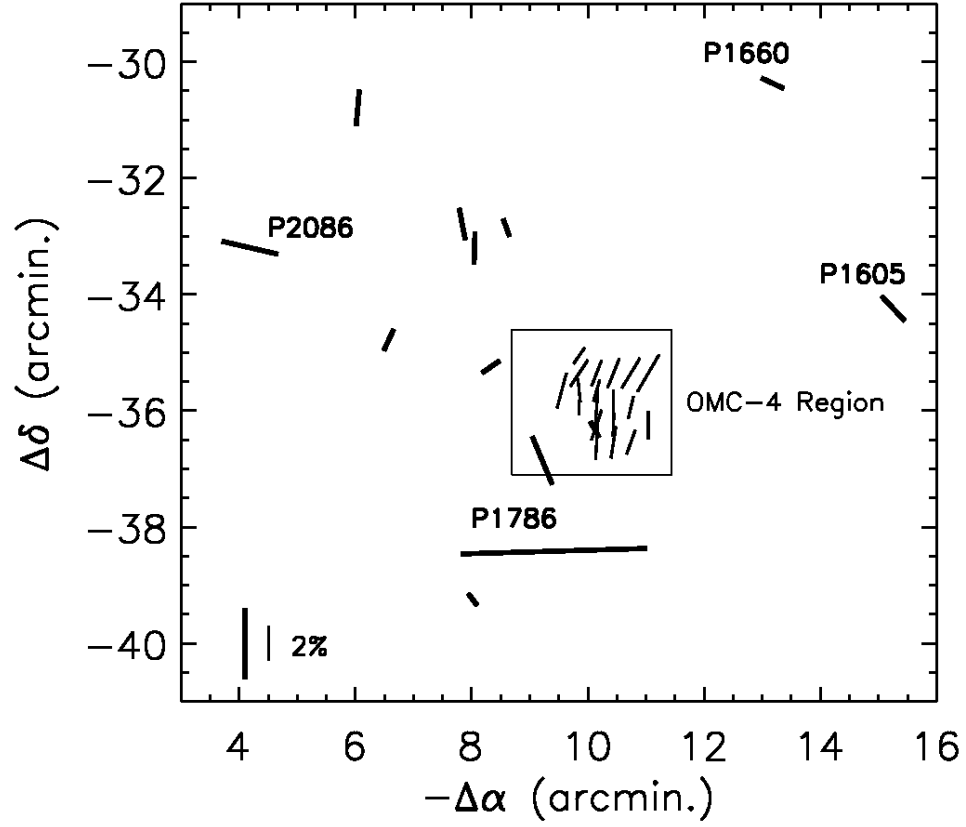


Fig. 20.— Map of $350\ \mu\text{m}$ data from Houde et al. (2004) (thin vectors) superimposed on visible data (bold vectors). Polarization scales are given in the bottom left. The reference position is R.A.= $5^{\text{h}}35^{\text{m}}48.0^{\text{s}}$, decl.= $-5^{\circ}00^{\text{mn}}00.0^{\text{s}}$ (J2000.0).

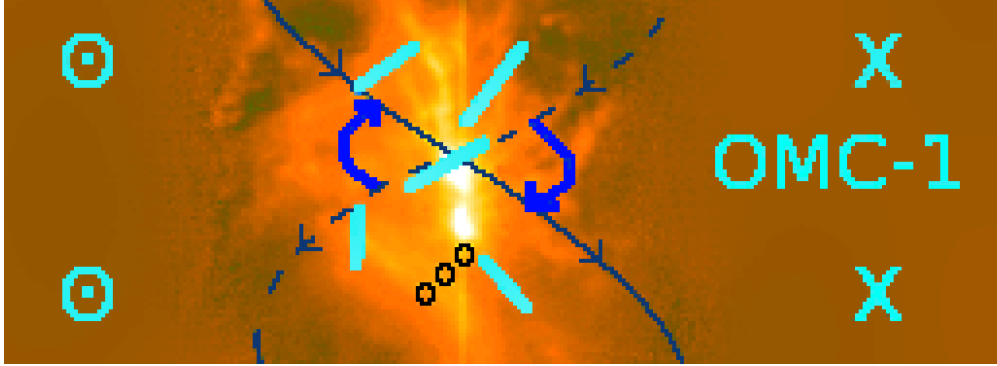


Fig. 21.— A schematic view of the magnetic field that could be wrapping the OMC-1 filament. The $850\ \mu\text{m}$ map of Johnstone & Bally (1999) is used to show the ISF. The symmetry axis of the two large scale magnetic field components seen in the $350\ \mu\text{m}$ data is suggested by the vertical translucent line. The morphology of the large scale magnetic field pervading OMC-1 is shown by the large scale two component structure. The foreground component is shown by a full line while the background component is shown with a dashed line. The drawn by eye green-blue vectors show the mean orientation of the magnetic field probed by submm data in several subregions. The black circles indicate regions where the foreground and background magnetic field components probably cancel each other within OMC-1. The rotation that is produced when moving from the far region, i.e. OMC-1, toward us on the LOS is illustrated by the blue arrows. Such a magnetic field could be blended to the external field probed with Zeeman data (Heiles 1997). The field comes out of the figure on the east side (arrows) and goes into it on the west side (crosses).

Table 1. New visible polarization data from the OMM.

Parenago	HD	$\alpha(2000)$ (^h ^m ^s)	$\delta(2000)$ ([°] ['] ^{''})	P_R (%)	σ_{P_R} (%)	θ_R ([°])	σ_{θ_R} ([°])	$\frac{P}{\sigma_P} > 3$	A_V (Mag.)	Distance (pc)	SC ^(a)
(1)	(2)	(3)	(4)	(5)	(6)	(7)	(8)	(9)	(10)	(11)	(12)
P1374	...	05 34 11.13	-05 22 54.6	0.29	0.10	59.3	10.3	0	?	?	0
P1539	...	05 34 40.04	-05 10 07.1	5.34	0.13	95.7	0.7	1	1.94	?	2
P1587	...	05 34 45.20	-05 25 04.1	2.53	0.17	91.7	1.9	1	?	?	?
P1659	...	05 34 55.98	-05 23 13.1	0.78	0.12	69.4	4.3	1	?	?	2
P1665b	...	05 34 51.5	-05 13.5	2.14	0.41	49.1	5.4	1	?	?	2
P1665	...	05 34 56.82	-05 11 33.5	0.26	0.21	40.4	23.1	0	2.15	?	0
P1684	...	05 35 00.11	-05 23 01.9	0.27	0.17	115.7	17.4	0	?	?	0
P1746	...	05 35 05.64	-05 25 19.5	1.11	0.13	64.6	3.5	1	?	?	?
P1763	...	05 35 07.53	-05 36 19.3	0.51	0.14	29.1	7.6	1	?	?	?
P1773	...	05 35 09.07	-05 29 59.2	0.30	0.14	59.6	13.4	0	?	?	0
P1775	...	05 35 07.5	-06 09 59.0	0.77	0.08	52.7	3.1	1	1.74	?	2
P1786	...	05 35 10.34	-05 38 24.9	5.26	0.11	91.7	0.6	1	?	?	?
P1802	...	05 35 11.14	-05 36 51.2	1.47	0.17	22.6	3.3	1	?	?	?
P1810	...	05 35 12.23	-05 36 39.4	0.15	0.15	138.3	28.2	0	?	?	0
P1827	...	05 35 13.61	-05 32 51.1	0.53	0.13	20.2	6.9	1	?	?	?
P1828	...	05 35 12.83	-05 39 34.3	0.19	0.17	142.9	26.4	0	?	?	0
P1835	...	05 35 15.79	-05 00 33.5	0.49	0.21	138.4	12.3	0	1.65	?	0
P1874	...	05 35 15.80	-05 33 12.3	0.93	0.16	178.2	4.9	1	?	?	?
P1876	...	05 35 14.68	-05 35 14.7	0.61	0.12	124.5	5.4	1	?	?	?
P1897	...	05 35 16.65	-05 32 47.4	0.92	0.21	10.9	6.5	1	?	?	?
P1898	...	05 35 15.92	-05 39 14.8	0.43	0.14	37.5	9.1	1	?	?	?
P1977	...	05 35 21.7	-05 34 46.8	0.67	0.13	154.9	5.4	1	?	?	?
P2005	...	05 35 25.24	-05 09 27.6	0.21	0.13	57.9	17.5	0	1.17	?	0
P2006	...	05 35 25.63	-05 09 49.2	0.31	0.13	56.9	11.5	0	1.17	?	0
P2007	...	05 35 25.42	-05 10 48.0	0.84	0.24	176.7	8.2	0	?	?	?
P2029	...	05 35 26.75	-05 11 07.1	1.49	0.18	25.9	3.5	1	?	?	?
P2030	...	05 35 26.88	-05 13 14.0	0.14	0.15	84.3	29.3	0	?	?	0
P2048	...	05 35 27.43	-05 35 19.4	0.91	0.35	36.6	10.9	0	?	?	0
P2057	...	05 35 28.92	-05 06 03.5	0.29	0.22	178.4	22.1	0	0.90	?	0
P2068	...	05 35 31.00	-05 04 14.8	0.14	0.13	69.8	27.8	0	1.12	?	0
P2119	...	05 35 35.98	-05 12 25.1	0.13	0.13	22.0	29.3	0	?	?	0
P2143	...	05 35 38.96	-05 08 55.9	0.34	0.14	36.7	11.8	0	0.98	?	0
P2164	...	05 35 42.91	-05 20 13.3	0.07	0.11	43.8	44.8	0	?	?	0
P2173	...	05 35 42.78	-05 11 54.7	0.68	0.19	57.5	7.9	1	?	?	?
P2174	...	05 35 42.94	-05 13 45.2	v ^(b)					?	?	0
P2208	...	05 35 46.89	-05 18 01.6	11.85	0.16	64.1	0.4	1	?	?	2
P2216	...	05 35 47.68	-05 10 30.3	00.28	0.16	16.2	15.9	0	1.07	?	0
P2217	...	05 35 47.40	-05 16 57.8	7.87	0.15	65.1	0.5	1	?	?	2
P2244	...	05 35 51.64	-05 08 09.2	2.98	0.19	75.7	1.8	1	0.76	?	0
P2252	...	05 35 52.63	-05 06 56.7	0.27	0.14	78.2	14.7	0	0.76	?	0
P2317	...	05 36 04.36	-05 07 14.4	1.95	0.13	78.9	2.0	1	1.26	?	?

^(a)SC: Selection Code, indicates the reliability of polarization data for probing magnetic fields. SC = 1 or 2 for reliable data. SC = ? for data considered as less reliable, and SC = 0 for data considered as non reliable. See section 2.1.3 for details.

^(b)v: apparently variable star.

Table 2. Visible polarization data from stars observed at OMM, and from Breger (1976) and/or from the Heiles (2000) catalog.

Parenago	HD	$\alpha(2000)$ (^h ^{mn} ^s)	$\delta(2000)$ ([°] ['] ^{''})	P (%)	σ_P (%)	θ ([°])	σ_θ ([°])	$\frac{P}{\sigma_P} > 3$	A_V (Mag.)	Distance (pc)	SC ^(a)	
(1)	(2)	(3)	(4)	(5)	(6)	(7)	(8)	(9)	(10)	(11)	(12)	
P1391 ^(ISM)		05 34 15.20	-05 11 49.6	0.38 ^(M)	0.12	53.3	09.4	1	?	?	?	
...		0.07 ^(B)	0.12	89.0	48.9	0	0	
P1455 ^(ISM)		05 34 24.83	-05 22 05.1	0.15 ^(M)	0.12	41.3	23.2	0	?	?	0	
...		0.04 ^(B)	0.06	66.0	42.8	0	
P1507 ^(ISM)		05 34 34.47	-05 03 06.9	0.69 ^(M)	0.11	96.8	4.5	1	1.14	?	1	
...		0.55 ^(B)	0.05	102.0	2.5	1	
P1540 ^(ICD)		05 34 39.79	-05 24 25.7	0.79 ^(M)	0.11	79.3	4.1	1	?	?	1	
...		1.11 ^(B)	0.10	85.0	2.6	1	
P1562 ^(ISM)	36899	05 34 42.28	-05 07 14.6	0.35 ^(M)	0.12	50.2	9.9	0	1.59	602.9	0	
...	0.89 ^(H)	0.03	171.0	1.0	1	
...	0.27 ^(B)	0.08	88.0	8.4	1	
P1575 ^(ISM)		05 34 43.54	-05 18 27.2	0.21 ^(M)	0.16	86.0	21.6	0	?	?	0	
...		0.18 ^(B)	0.09	89.0	14.3	0	
P1605 ^(ICD)	36917	05 34 46.98	-05 34 14.6	1.06 ^(M)	0.11	44.6	3.0	1	0.62	239.9	1	
...	0.97 ^(H)	0.03	43.0	0.9	1	
...	0.84 ^(B)	0.05	42.0	1.7	1	
P1623 ^(ICD)		05 34 49.99	-05 18 44.7	2.33 ^(M)	0.16	53.6	1.9	1	?	?	1	
...		1.83 ^(B)	0.04	52.0	0.6	1	
P1660 ^(ISM)	36939	05 34 55.29	-05 30 22.1	0.49 ^(M)	0.10	61.2	5.9	1	0.31	524.8	1	
...	0.71 ^(H)	0.03	65.0	1.3	1	
...	0.53 ^(B)	0.07	53.0	3.8	1	
P1683 ^(ICD)		05 35 00.73	-05 05 11.0	1.42 ^(M)	0.13	108.0	2.6	1	1.48	?	1	
...		1.36 ^(B)	0.07	117.0	1.5	1	
P1685 ^(ICD)		05 35 00.14	-05 25 16.3	1.41 ^(M)	0.10	78.7	2.1	1	?	?	1	
...		1.48 ^(B)	0.07	67.0	1.4	1	
P1712 ^(ICD)		05 35 03.62	-05 05 44.5	3.44 ^(M)	0.12	100.2	1.0	1	1.48	?	1	
...	3.73 ^(B)	0.09	100.0	0.7	1	
P1724 ^(ICD)		05 35 04.3	-05 08 12.8	1.11 ^(M)	0.10	83.0	2.6	1	1.51	?	1	
...	1.50 ^(B)	0.04	79.0	0.8	1	
P1744 ^(ISM)	36981	05 35 06.20	-05 12 15.9	0.14 ^(M)	0.10	49.6	20.8	0	?	?	0	
...	0.07 ^(H)	0.03	84.0	13.0	0	0	
...	0.36 ^(B)	0.07	81.0	5.5	1	?	
P1885 ^(ICD)		05 35 16.99	-05 21 45.6	1.80 ^(M)	0.13	107.5	2.0	1	?	?	1	
...	0.98 ^(B)	0.08	105.0	2.3	1	?	?	...	
...	0.06 ^(B)	0.15	162.0	71.2	0	
P1905 ^(ISM)	37019	05 35 18.20	-05 03 54.9	v ^(b) (M)	0.35 ^(H)	0.03	96.0	2.6	1	1.43	436.5	0
...	0.28 ^(B)	0.08	48.0	8.2	1	
...	0.28 ^(B)	0.08	48.0	8.2	1	
P1950 ^(ISM)		05 35 23.4	-04 53 01	0.63 ^(M)	0.15	40.1	6.7	1	?	?	0	
...		0.29 ^(B)	0.08	70.0	7.9	1	
P1953 ^(ISM)		05 35 21.23	-05 09 16.1	0.24 ^(M)	0.13	22.3	15.0	0	?	?	0	
...		0.26 ^(B)	0.10	66.0	11.0	0	
P1956 ^(ICD)		05 35 20.65	-05 21 44.9	1.93 ^(M)	0.09	37.9	1.4	1	?	?	1	
...		1.30 ^(B)	0.07	40.0	1.5	1	
P2031 ^(ISM)	37042	05 35 26.40	-05 25 00.7	0.37 ^(M)	0.10	140.7	7.4	1	0.62	757.0	1	
...	0.56 ^(H)	0.03	139.0	1.6	1	
...	0.27 ^(B)	0.04	135.0	4.2	1	

Table 2—Continued

Parenago	HD	$\alpha(2000)$ (^h ^m ^s)	$\delta(2000)$ ([°] ['] ^{''})	P (%)	σ_P (%)	θ ([°])	σ_θ ([°])	$\frac{P}{\sigma_P} > 3$	A_V (Mag.)	Distance (pc)	SC ^(a)
(1)	(2)	(3)	(4)	(5)	(6)	(7)	(8)	(9)	(10)	(11)	(12)
P2043 ^(ISM)		05 35 28.5	-04 55 03.2	0.12 ^(M)	0.15	68.0	34.2	0	?	?	0
...		0.34 ^(B)	0.17	60.0	14.2	0
P2065 ^(ISM)	37059	05 35 31.16	-04 54 15.4	0.21 ^(M)	0.10	48.9	13.3	0	0.31	602.6	0
...	0.75 ^(H)	0.03	86.0	1.2	1
...	0.08 ^(B)	0.05	118.0	17.8	0
P2074 ^(ICD)	37061	05 35 31.36	-05 16 02.6	1.65 ^(M)	0.08	59.4	1.4	1	?	?	1
...	1.37 ^(B)	0.05	62.0	1.0	1
P2102 ^(ISM)	37060	05 35 34.28	-05 06 21.2	0.16 ^(M)	0.11	71.1	19.4	0	0.82	?	0
...	0.30 ^(B)	0.14	74.0	13.3	0
P2284 ^(ISM)	37114	05 35 58.53	-05 22 31.6	0.18 ^(M)	0.10	42.5	15.0	0	0.31	559.0	0
...	0.39 ^(H)	0.03	88.0	2.3	1	1
...	0.31 ^(B)	0.10	69.0	9.2	1	1
P2290 ^(ISM)	294266	05 36 00.70	-04 57 57.1	0.18 ^(M)	0.12	25.8	18.5	0	1.82	?	0
...	0.13 ^(B)	0.08	175.0	17.5	0
P2342 ^(ISM)	37142	05 36 11.02	-05 03 41.5	0.35 ^(M)	0.11	54.8	8.9	1	1.64	?	2
...	0.15 ^(B)	0.08	45.0	15.2	0	0
P2387 ^(ISM)	37174	05 36 27.19	-05 24 31.3	0.29 ^(M)	0.09	60.3	9.0	1	2.05	524.8	0
...	0.33 ^(H)	0.03	156.0	2.8	1
...	0.06 ^(B)	0.15	162.0	71.2	0

^(ISM)Polarization mainly produced by ISM dust (see Breger 1976).

^(ICD)Polarization mainly produced by ICD (see Breger 1976).

^(a)SC: Selection Code, indicates the reliability of polarization data for probing magnetic fields. SC = 1 or 2 for reliable data. SC = ? for data considered as less reliable, and SC = 0 for data considered as non reliable. See section 2.1.3 for details.

^(b)v: apparently variable star.

^(B)Data from Breger (1976), see also Breger (1977) where the origin of the polarization is discussed for some stars. The effective wavelength of observations lies between B and V effective wavelength.

^(H)Data from Heiles (2000); λ is not defined precisely.

^(M)Data from Mont-Mégantic Observatory.

Table 3. Supplementary visible polarization data from Breger (1976) and from the Heiles (2000) catalog.

Parenago	HD	$\alpha(2000)$ (^h ^m ^s)	$\delta(2000)$ ([°] ['] ^{''})	P (%)	σ_P (%)	θ ([°])	σ_θ ([°])	$\frac{P}{\sigma_P} > 3$	A_V (Mag.)	distance (pc)	SC ^(a)
(1)	(2)	(3)	(4)	(5)	(6)	(7)	(8)	(9)	(10)	(11)	(12)
P1036 ^(ICD)		05 32 55.89	-04 32 42.7	2.33 ^(B)	0.10	95.0	1.2	1	0.49	?	2
P1044 ^(ICD)	36629	05 32 57.08	-04 33 59.3	1.96 ^(B)	0.02	97.0	0.3	1	0.64	719.0	1
...	1.84 ^(H)	0.05	95.8	0.7	1
P1049 ^(ICD)		05 32 58.00	-04 30.8	2.34 ^(B)	0.14	108.0	1.7	1	0.49	?	1
P1073 ^(ICD)		05 33 00.0	-06 10.1	3.97 ^(B)	0.29	36.0	2.1	1	0.20	?	?
P1097 ^(ISM)	36655	05 33 07.48	-05 20 26.1	0.50 ^(H)	0.03	47.0	1.8	1	1.18	478.6	0
...	0.37 ^(B)	0.05	76.0	3.9	1
P1117 ^(ISM)	36671	05 33 14.03	-04 38 07.2	0.39 ^(H)	0.03	82.0	2.3	1	1.22	316.2	1
...	0.49 ^(B)	0.08	100.0	4.7	1
P1122 ^(ICD)		05 33 16.0	-04 28.2	1.41 ^(B)	0.12	81.0	2.4	1	0.44	?	2
P1150 ^(ICD)		05 33 20.07	-05 06 24.3	5.91 ^(B)	0.06	97.0	0.3	1	1.45	?	1
P1175 ^(ICD)		05 33 24.3	-05 21 16	0.57 ^(B)	0.06	98.0	3.0	1	1.47	?	2
P1212 ^(ICD)	294224	05 33 34.06	-05 05 01.7	4.21 ^(B)	0.06	87.0	0.4	1	1.39	?	1
P1427 ^(ICD)		05 34 22.26	-04 57 40.2	1.03 ^(B)	0.18	32.0	5.0	1	1.52	?	?
P1466 ^(ICD)		05 34 24.9	-06 01 03	1.12 ^(B)	0.11	61.0	2.8	1	1.29	?	?
P1491 ^(ISM)	36865	05 34 32.43	-04 29 14.8	0.14 ^(H)	0.03	68.0	6.5	1	0.31	281.0	1
...	0.17 ^(B)	0.04	77.0	6.7	1
P1526 ^(ICD)		05 34 41.0	-04 17.5	1.57 ^(B)	0.06	104.0	1.1	1	0.54	?	2
P1546 ^(ISM)	36883	05 34 43.20	-04 23 31.5	0.23 ^(H)	0.03	41.0	4.0	1	0.26	521.0	1
...	0.22 ^(B)	0.10	48.0	13.0	0
P1567 ^(ICD)		05 34 44.5	-04 42 14	2.33 ^(B)	0.23	97.0	2.8	1	2.10	?	2
P1581 ^(ICD)		05 34 48	-04 17.5	2.27 ^(B)	0.12	123.0	1.5	1	0.45	?	2
P1628	36916	05 34 53.96	-04 06 37.5	0.27 ^(H)	0.03	58.0	3.4	1	0.89	356.0	2
P1654 ^(ICD)	36938	05 34 56.24	-04 45 57.4	0.90 ^(H)	0.03	44.0	1.0	1	0.62	478.6	0
...	0.62 ^(B)	0.10	22.0	4.6	1
P1664 ^(ISM)	36936	05 34 59.00	-04 21 15.4	0.18 ^(H)	0.03	48.0	5.1	1	0.26	512.0	2
P1698 ^(ISM)	36957	05 35 03.73	-04 23 06.1	0.19 ^(H)	0.03	84.0	4.8	1	0.32	398.1	0
...	0.50 ^(B)	0.07	55.0	4.0	1
P1708 ^(ISM)	36958	05 35 04.79	-04 43 54.6	0.94 ^(H)	0.08	47.7	2.3	1	0.62	511.0	1
...	0.59 ^(B)	0.06	38.0	2.9	1
P1716 ^(ISM)	36959	05 35 01.01	-06 00 33.4	0.16 ^(H)	0.0	82.0	0.0	1	0.31	646.0	0
...	0.19 ^(B)	0.04	131.0	6.0	1
P1719 ^(ICD)		05 35 05.42	-04 43 19.8	0.73 ^(B)	0.06	116.0	2.4	1	?	?	?
P1728 ^(ISM)	36960	05 35 02.68	-06 00 07.3	0.11 ^(H)	0.0	69.0	0.0	1	0.31	539.0	1
...	0.13 ^(B)	0.03	70.0	6.6	1
P1736 ^(ICD)		05 35 37.58	-05 16 44.5	1.73 ^(B)	0.16	123.0	2.7	1	?	?	?
P1772 ^(ICD)	36982	05 35 09.84	-05 27 53.3	0.55 ^(B)	0.03	64.0	1.6	1	1.24	1139.0	1
...	1.01 ^(H)	0.02	56.0	0.6	1
P1795 ^(ICD)	36998	05 35 13.23	-04 37 34.6	0.27 ^(H)	0.03	169.0	3.4	1	1.70	575.4	0
...	0.30 ^(B)	0.05	63.0	4.8	1
P1798 ^(ICD)	294264	05 35 13.35	-04 51 44.9	2.62 ^(B)	0.08	77.0	0.9	1	?	?	1
P1799 ^(ICD)		05 35 11.64	-05 16 57.8	5.84 ^(B)	0.12	134.0	0.6	1	?	?	1
P1813 ^(ISM)	37000	05 35 11.01	-05 55 36.9	0.35 ^(H)	0.03	84.0	2.6	1	0.31	465.0	?
...	0.07 ^(B)	0.03	96.0	12.2	0	0
P1854 ^(ICD)	294263	05 35 17.83	-04 41 07.0	0.63 ^(B)	0.08	71.0	3.6	1	?	?	?
P1881 ^(ICD)	36998	05 35 18.42	-04 40 55.9	1.03 ^(B)	0.05	107.0	1.4	1	?	?	1
P1901 ^(ISM)	37025	05 35 15.75	-06 01 57.9	0.06 ^(H)	0.03	99.0	15.2	0	1.60	?	0

Table 3—Continued

Parenago	HD	$\alpha(2000)$ (^h ^m ^s)	$\delta(2000)$ ([°] ['] ^{''})	P (%)	σ_P (%)	θ ([°])	σ_θ ([°])	$\frac{P}{\sigma_P} > 3$	A_V (Mag.)	distance (pc)	SC ^(a)
(1)	(2)	(3)	(4)	(5)	(6)	(7)	(8)	(9)	(10)	(11)	(12)
...	0.16 ^(B)	0.02	60.0	3.6	1	?
P1921 ^(ICD)	...	05 35 18.91	-05 16 14.1	1.41 ^(B)	0.33	169.0	6.7	1	?	?	?
P1932 ^(ISM)	37016	05 35 22.32	-04 25 27.6	0.35 ^(H)	0.0	55.0	0.0	1	0.74	345.0	0
...	0.36 ^(B)	0.08	29.0	6.3	1
P1933 ^(ISM)	37017	-05 35 21.8	-04 29 39.0	0.25 ^(H)	0.0	51.0	0.0	1	0.96	630.0	1
...	0.40 ^(B)	0.08	49.0	5.7	1
P1970 ^(ISM)	37018	05 35 23.16	-04 50 18.1	0.47 ^(H)	0.03	62.0	2.2	1	0.31	470.0	0
...	0.31 ^(B)	0.05	151.0	4.6	1
P1993 ^(ICD)	37041	05 35 22.90	-05 24 57.8	0.79 ^(H)	0.05	95.8	1.8	1	0.62	607.0	1
...	0.96 ^(B)	0.02	99.0	0.6	1
P2001 ^(ICD)	...	05 35 23.84	-05 30 47.5	1.02 ^(B)	0.16	175.0	4.5	1	?	?	?
P2037 ^(ISM)	37043	05 35 25.98	-05 54 35.6	0.11 ^(H)	0.0	61.0	0.0	1	0.31	451.0	0
...	0.21 ^(B)	0.04	133.0	5.4	1
P2054	37040	05 35 31.08	-04 21 50.6	0.23 ^(H)	0.0	61.0	0.0	1	0.95	500.0	?
P2085 ^(ISM)	37062	05 35 31.44	-05 25 16.4	0.41 ^(H)	0.03	162.0	2.2	1	1.86	689.0	0
...	0.14 ^(B)	0.06	47.0	12.2	0
P2086 ^(ICD)	...	05 35 31.25	-05 33 11.8	1.63 ^(B)	0.08	77.0	1.4	1	?	?	1
P2185 ^(ICD)	...	05 35 43.22	-05 36 27.6	0.90 ^(B)	0.15	114.0	4.8	1	?	?	?
P2233 ^(ICD)	...	05 35 50.7	-04 51 11	3.09 ^(B)	0.11	123.0	1.0	1	1.71	?	?
P2248 ^(ICD)	...	05 35 49.83	-05 40 27.6	3.13 ^(B)	0.08	90.0	0.7	1	?	?	?
P2261 ^(ICD)	...	05 35 54.9	-04 58 07.0	1.05 ^(B)	0.12	40.0	3.3	1	2.17	?	?
P2271 ^(ISM)	37115	05 35 54.08	-05 37 42.3	0.37 ^(H)	0.03	89.0	2.5	1	0.31	304.0	1
...	0.31 ^(B)	0.07	105.0	6.4	1
P2302 ^(ICD)	37130	05 36 03.57	-04 45 07.6	1.02 ^(B)	0.12	136.0	3.4	1	1.94	?	2
P2310 ^(ICD)	...	05 36 04.3	-04 44 39.0	3.83 ^(B)	0.09	133.0	0.7	1	1.94	?	2
P2314 ^(ISM)	37129	05 36 06.26	-04 25 32.8	0.32 ^(H)	0.03	64.6	2.6	1	1.05	631.0	1
...	0.23 ^(B)	0.04	53.0	5.0	1
P2368 ^(ICD)	...	05 36 16.98	-05 11 42.9	4.69 ^(B)	0.50	20.0	3.0	1	1.62	?	?
P2425 ^(ICD)	...	05 36 38.7	-05 28 22	3.47 ^(B)	0.06	92.0	0.5	1	2.02	?	1
P2448 ^(ICD)	...	05 36 53.63	-04 39 53.5	2.13 ^(B)	0.09	155.0	1.2	1	1.73	?	?
P2467 ^(ICD)	...	05 37 02.0	-04 12.3	1.62 ^(B)	0.15	73.0	2.6	1	0.61	?	?
P2471 ^(ICD)	...	05 37 03.14	-04 37 02.5	0.93 ^(B)	0.17	44.0	5.2	1	1.53	?	?
P2500 ^(ICD)	...	05 37 13.43	-05 40 26.9	1.79 ^(B)	0.02	87.0	0.3	1	2.06	?	2
P2519 ^(ICD)	...	05 37 21.0	-04 40.4	2.39 ^(B)	0.08	155.0	1.0	1	1.91	?	1
P2579 ^(ICD)	...	05 37 41.41	-04 51 04.1	1.92 ^(B)	0.11	114.0	1.6	1	1.38	?	?
P2602 ^(ICD)	37356	05 37 53.39	-04 48 50.5	1.45 ^(H)	0.06	70.2	1.2	1	1.08	489.0	1
...	1.51 ^(B)	0.03	75.0	0.6	1
P2609 ^(ICD)	294295	05 37 55.86	-04 47 18.0	0.75 ^(B)	0.01	76.0	0.4	1	1.08	?	2
P2653	...	05 38 14.51	-05 25 13.3	0.23 ^(H)	0.03	57.0	4.0	1	2.10	478.6	?
P2701	37469	05 38 39.46	-04 40 48.8	2.22 ^(H)	0.03	108.0	0.4	1	1.02	501.2	?
P2758	...	05 39 02.4	-05 11 40.1	0.31 ^(H)	0.03	39.0	2.9	1	1.33	506.0	?

^(ISM)Polarization mainly produced by ISM dust (see Breger 1976).

^(ICD)Polarization mainly produced by ICD (see Breger 1976).

^(a)SC: Selection Code, indicates the reliability of polarization data for probing magnetic fields. SC = 1 or 2 for reliable data. SC = ? for data considered as less reliable, and SC = 0 for data considered as non reliable. See section 2.1.3 for details.

^(B)Data from Breger (1976), see also Breger (1977) where the origin of the polarization is discussed for some stars.

^(H)Data from Heiles (2000).

Table 4. Visible polarization data in OMC-2 from Mount Lemmon.

Star ^(a)	$\alpha(2000)$ (^h ^m ^s)	$\delta(2000)$ ([°] ['] ^{''})	P_V (%)	σ_{P_V} (%)	θ_V ([°])	σ_{θ_V} ([°])	P_R (%)	σ_{P_R} (%)	θ_R ([°])	σ_{θ_R} ([°])	P_I (%)	σ_{P_I} (%)	θ_I ([°])	σ_{θ_I} ([°])	A_V (Mag.)	SC ^(b)
(1)	(2)	(3)	(4)	(5)	(6)	(7)	(8)	(9)	(10)	(11)	(12)	(13)	(14)	(15)	(16)	(17)
26	5 35 03.8	-5 08 16.8	1.38	0.12	80.0	2.5	1.30	0.06	81.0	1.3	1.03	0.06	1.7	1.7	1.51	?
76	5 35 21.3	-5 12 09.1	0.86	0.13	18.3	4.3	0.74	0.08	13.1	3.1	0.65	0.08	14.5	3.5	?	1
85	5 35 22.3	-5 09 11.2	0.45	0.14	63.8	8.9	1.14	?
111	5 35 25.6	-5 09 48.4	0.88	0.11	84.5	3.6	0.69	0.21	68.0	8.7	1.17	1
112	5 35 26.1	-5 08 40.4	0.42	0.13	58.7	8.9	0.18	0.06	79.7	9.5	1.17	1
116	5 35 26.9	-5 11 04.5	3.57	0.18	49.3	1.4	3.33	0.16	52.0	1.4	?	1
117	5 35 27.0	-5 13 08.5	0.31	0.09	48.9	8.3	?	?
139	5 35 31.9	-5 09 26.8	0.51	0.14	74.3	7.9	0.54	0.12	60.7	6.3	0.68	0.11	52.5	4.6	0.98	1
175	5 35 40.7	-5 08 59.5	8.83	0.34	73.2	1.1	8.20	0.26	73.8	0.9	0.98	0
183	5 35 43.0	-5 11 47.7	0.54	0.11	83.1	5.8	?	?
191	5 35 44.9	-5 07 16.8	0.20	0.06	29.8	8.6	0.65	?
198	5 35 47.6	-5 10 24.0	0.35	0.12	76.7	9.8	0.34	0.12	73.4	10.1	1.07	1
207	5 35 51.0	-5 09 26.2	8.04	0.33	74.1	1.2	3.80	0.09	74.1	0.7	1.06	0
217	5 35 56.2	-5 08 58.6	4.69	0.37	97.4	2.3	1.06	0

^(a)Numbers are from Jones et al. (1994)

^(b)SC: Selection Code, indicates the reliability of polarization data for probing magnetic fields. SC = 1 or 2 for reliable data. SC = ? for data considered as less reliable, and SC = 0 for data considered as non reliable. See section 2.1.3 for details.

Table 5. IR polarization data in the BN region.

Star number (1)	$\alpha(2000)$ (^h ^m ^s) (2)	$\delta(2000)$ ([°] ['] ^{''}) (3)	$P_K^{(a)}$ (%) (4)	θ_K ([°]) (5)	σ_{θ_K} ([°]) (6)	$H - K$ (Mag.) (7)	LBSL ^(b) (8)	S&S ^(c) (9)	Other ID ^(d) (10)	θ_{off} ([°]) (11)	τ_K (12)	SC ^(e) (13)
0	5 35 16.2	-5 21 54.2	6.8	71.0	1.3	0.48	0.27	0
1	5 35 15.9	-5 21 51.2	1.4	102.0	6.1	0.47	75	0.25	1
2	5 35 15.0	-5 21 51.5	2.6	81.0	3.3	0.84	48	0.81	1
3	5 35 14.7	-5 21 53.6	5.0	145.0	1.7	1.69	71	2.08	1
4	5 35 15.2	-5 21 59.0	5.1	110.0	1.7	1.22	79	1.38	1
5	5 35 15.0	-5 22 02.8	0.9	61.0	9.5	0.19	-0.16	0
8	5 35 13.9	-5 22 02.8	7.8	144.0	1.1	2.34	73	3.06	1
9	5 35 13.2	-5 21 57.1	5.3	116.0	1.6	1.09	77	1.18	1
11	5 35 14.6	-5 22 09.0	3.8	46.0	2.3	0.34	s	0.06	0
12	5 35 13.9	-5 22 09.6	1.8	56.0	4.8	0.53	h	...	P1089	19	0.34	1
13	5 35 16.1	-5 22 12.0	2.2	66.0	3.9	1.29	46	1.48	1
14	5 35 16.0	-5 22 13.9	1.1	60.0	7.8	0.80	37	0.75	1
15	5 35 15.3	-5 22 16.9	2.1	65.0	4.1	1.21	y	36	1.36	1
16	5 35 13.9	-5 22 18.7	11.2	108.0	0.8	2.12	75	2.73	1
17	5 35 13.2	-5 22 16.9	3.0	42.0	2.9	0.45	a	0.22	0
18	5 35 13.4	-5 22 22.3	2.6	24.0	3.3	1.05	b	CB1	...	9	1.12	1
19	5 35 13.7	-5 22 20.9	4.1	93.0	2.1	0.61	e	0.46	0
20	5 35 13.9	-5 22 22.8	1.8	32.0	4.8	0.74	g	2	0.66	1
21	5 35 13.5	-5 22 26.8	1.3	62.0	6.6	0.72	c	30	0.63	1
22	5 35 16.2	-5 22 22.0	1.1	72.0	7.8	0.94	52	0.96	1
23	5 35 15.8	-5 22 21.7	1.1	68.0	7.8	1.10	48	1.20	1
24	5 35 15.3	-5 22 25.5	9.5	74.0	0.9	0.83	z	0.79	0
25	5 35 15.2	-5 22 24.4	8.9	70.0	1.0	0.46	0.24	0
26	5 35 14.9	-5 22 31.4	15.4	51.0	0.6	0.48	u	0.27	0
27	5 35 14.8	-5 22 29.8	20.7	141.0	0.4	3.73	...	CB4	...	70	5.14	1
30	5 35 14.7	-5 22 33.3	1.3	58.0	6.6	0.34	t	...	P1839	...	0.06	0
31	5 35 14.4	-5 22 32.5	2.3	80.0	3.7	2.37	n	n	...	48	3.10	1
33	5 35 15.2	-5 22 36.0	9.2	141.0	0.9	2.58	x	68	3.42	1
34	5 35 14.9	-5 22 38.2	0.6	41.0	14.3	0.57	v	...	P1840	12	0.40	1
35	5 35 15.8	-5 22 44.1	1.8	28.0	4.8	0.13	-0.25	0
36	5 35 15.4	-5 22 46.5	2.2	26.0	3.9	0.37	0.10	0
37	5 35 14.7	-5 22 47.4	3.3	33.0	2.6	1.37	4	1.60	1
38 (BN)	5 35 14.2	-5 22 23.6	18.0	115.0	0.5	3.86	BN	...	IRc1	82	5.34	1

^(a)A precision $\sigma_P = \pm 0.3\%$ can be assumed for these data.

^(b)Lonsdale et al. (1982)

^(c)See Stolovy et al. (1998) and Shuping et al. (2004)

^(d)ID:Identification Designation

^(e)SC:Selection Code, indicates the reliability of polarization data to probe magnetic fields. SC = 1 for reliable data. SC= 0 otherwise.

Table 6. Means and dispersions of polarization and position angles at various wavelengths and various scales in and around regions Orion A, OMC-1 and BN.

	Data set	Large scale region (Figure 12) ($\approx 1.5^\circ \times 2.1^\circ$)	OMC-1 region (Figure 13) ($\approx 21' \times 17'$)	BN region (Figure 14) ($\approx 1.5' \times 1.5'$)
(1)	(2)	(3)	(4)	(5)
$\overline{P}_V \pm S_{P_V} (^\circ)^{(a)}$	(b)	1.83 ± 2.06 ($N^{(e)}=61$)	2.38 ± 2.87 ($N = 20$)	1.8 ± 0.0 ($N = 1$)
$\overline{P}_V \pm S_{P_V} (^\circ)^{(a)}$	$(P \geq 1\%)^{(c)}$	2.87 ± 2.27 ($N = 34$)	2.94 ± 3.13 ($N = 15$)	...
$\overline{P}_V \pm S_{P_V} (^\circ)^{(a)}$	$(P < 1\%)^{(d)}$	0.52 ± 0.28 ($N = 27$)	0.68 ± 0.22 ($N = 5$)	...
$\overline{P}_{2.2\mu\text{m}} \pm S_{P_{2.2\mu\text{m}}} (^\circ)$	(b)	4.89 ± 5.47 ($N = 22$)
$\overline{P}_{350\mu\text{m}} \pm S_{P_{350\mu\text{m}}} (^\circ)$	(b)	...	2.65 ± 1.48 ($N = 470$)	2.18 ± 0.42 ($N = 25$)
$\overline{\theta}_V \pm S_{\theta_V} (^\circ)^{(a)}$	(b)	79.7 ± 30.0 ($N = 61$)	63.6 ± 38.9 ($N = 20$)	107.5 ± 0.0 ($N = 1$)
$\overline{\theta}_V \pm S_{\theta_V} (^\circ)^{(a)}$	$(P \geq 1\%)^{(c)}$	89.6 ± 27.8 ($N = 34$)	66.1 ± 40.3 ($N = 15$)	...
$\overline{\theta}_V \pm S_{\theta_V} (^\circ)^{(a)}$	$(P < 1\%)^{(d)}$	67.3 ± 28.3 ($N = 27$)	92.1 ± 29.6 ($N = 5$)	...
$\overline{\theta}_{2.2\mu\text{m}} \pm S_{\theta_{2.2\mu\text{m}}} (^\circ)$	(b)	84.6 ± 38.5 ($N = 22$)
$\overline{\theta}_{350\mu\text{m}} \pm 90^\circ \pm S_{\theta_{350\mu\text{m}}} (^\circ)$	(b)	...	111.6 ± 30.1 ($N = 470$)	119.7 ± 8.7 ($N = 25$)

(a) Include data from Tables 1, 2, 3 and 4.

(b) No threshold on the degrees of polarization.

(c) Only data with $P \geq 1\%$ are considered.

(d) Only data with $P < 1\%$ are considered.

(e) N : number of measurements in the set considered.

Table 7. Means and dispersions of polarization and position angles at various wavelengths and various scales in and around regions OMC-2/3 and OMC-4.

	Data set	OMC-2/3 region (Figure 18) ($\approx 26' \times 30'$)	OMC-2/3 inner region (Figure 19) ($\approx 3' \times 5.5'$)	OMC-4 region (Figure 20) ($\approx 14' \times 14'$)
(1)	(2)	(3)	(4)	(5)
$\overline{P}_V \pm S_{P_V} (^{\circ})^{(a)}$	(b)	2.15 ± 2.50 ($N^{(e)}=34$)	1.00 ± 1.03 ($N = 9$)	1.20 ± 1.27 ($N = 13$)
$\overline{P}_V \pm S_{P_V} (^{\circ})^{(a)}$	$(P \geq 1\%)^{(c)}$	3.30 ± 2.72 ($N = 20$)	2.53 ± 1.47 ($N = 2$)	2.17 ± 1.74 ($N = 5$)
$\overline{P}_V \pm S_{P_V} (^{\circ})^{(a)}$	$(P < 1\%)^{(d)}$	0.50 ± 0.22 ($N = 14$)	0.56 ± 0.27 ($N = 7$)	0.60 ± 0.28 ($N = 8$)
$\overline{P}_{350\mu\text{m}} \pm S_{P_{350\mu\text{m}}} (^{\circ})$	(b)	1.79 ± 1.16 ($N = 137$)	1.41 ± 1.26 ($N = 52$)	1.66 ± 0.39 ($N = 19$)
$\overline{P}_{850\mu\text{m}} \pm S_{P_{850\mu\text{m}}} (^{\circ})$	(b)	2.82 ± 1.62 ($N = 251$)	1.98 ± 1.00 ($N = 91$)	...
$\overline{\theta}_V \pm S_{\theta_V} (^{\circ})^{(a)}$	(b)	66.3 ± 34.6 ($N = 34$)	46.9 ± 29.7 ($N = 9$)	54.5 ± 36.3 ($N = 13$)
$\overline{\theta}_V \pm S_{\theta_V} (^{\circ})^{(a)}$	$(P \geq 1\%)^{(c)}$	71.1 ± 37.7 ($N = 20$)	37.6 ± 16.6 ($N = 2$)	42.4 ± 40.4 ($N = 5$)
$\overline{\theta}_V \pm S_{\theta_V} (^{\circ})^{(a)}$	$(P < 1\%)^{(d)}$	59.4 ± 29.5 ($N = 14$)	49.6 ± 33.1 ($N = 7$)	39.5 ± 33.9 ($N = 8$)
$\overline{\theta}_{350\mu\text{m}} \pm 90^{\circ} \pm S_{\theta_{350\mu\text{m}}} (^{\circ})$	(b)	44.7 ± 24.6 ($N = 137$)	48.7 ± 32.7 ($N = 52$)	75.7 ± 12.6 ($N = 19$)
$\overline{\theta}_{850\mu\text{m}} \pm 90^{\circ} \pm S_{\theta_{850\mu\text{m}}} (^{\circ})$	(b)	55.5 ± 35.5 ($N = 251$)	69.0 ± 42.5 ($N = 91$)	...

^(a) Include data from Tables 1, 2, 3 and 4.

^(b) No threshold on the degrees of polarization.

^(c) Only data with $P \geq 1\%$ are considered.

^(d) Only data with $P < 1\%$ are considered.

^(e) N : number of measurements in the set considered.